CHARM SEMILEPTONIC DECAYS IN THE FOCUS EXPERIMENT

by

Eduardo E. Luiggi López

A Thesis submitted in partial fulfillment of the requirements for the degree of

MASTER OF SCIENCE

in

PHYSICS

UNIVERSITY OF PUERTO RICO

MAYAGÜEZ CAMPUS

2003

Approved by:

Angel M. López, Ph.D. President, Graduate Committee	Date
Héctor Méndez, Ph.D. Member, Graduate Committee	Date
Huimin Liu, Ph.D. Member, Graduate Committee	Date
Wolfgang Rolke, Ph.D. Representative of Graduate Studies	Date
Dorial Castellanos, Ph.D. Chairperson of Physics Department	Date

Abstract

Using data collected by FOCUS, a fixed target experiment at Fermi National Accelerator Laboratory (Fermilab), we present new measurements for the vector meson semileptonic branching ratios $\frac{\Gamma(D^+\to\overline{K^{*0}}\mu^+\nu)}{\Gamma(D^+\to K^-\pi^+\pi^+)}$ and $\frac{\Gamma(D^+\to\rho^0\mu^+\nu)}{\Gamma(D^+\to\overline{K^{*0}}\mu^+\nu)}$. We found these branching ratios to be $0.595 \pm 0.008 \pm 0.014$ and $0.034 \pm 0.005 \pm 0.005$ respectively. Using these values, we report $\Gamma(D^+ \to \overline{K^{*0}} l^+\nu) = (5.48 \pm 0.39) \times 10^{10} sec^{-1}$ and $\Gamma(D^+ \to \rho^0\mu^+\nu) = (0.17 \pm 0.03) \times 10^{10} sec^{-1}$.

Resumen

Utilizando datos tomados por FOCUS, un experimento de blanco fijo en Fermi National Accelerator Laboratory (Fermilab), presentamos nuevas medidas para las fracciones de decaimiento $\frac{\Gamma(D^+\to\overline{K^{*0}}\mu^+\nu)}{\Gamma(D^+\to K^-\pi^+\pi^+)}$ y $\frac{\Gamma(D^+\to\rho^0\mu^+\nu)}{\Gamma(D^+\to\overline{K^{*0}}\mu^+\nu)}$. Encontramos que estas fracciones de decaimientos son $0.595 \pm 0.008 \pm 0.014$ y $0.034 \pm 0.005 \pm 0.005$ respectivamente. Usando estos valores, reportamos $\Gamma(D^+ \to \overline{K^{*0}} l^+\nu) = (5.48 \pm 0.39) \times 10^{10} sec^{-1}$ y $\Gamma(D^+ \to \rho^0\mu^+\nu) = (0.17 \pm 0.03) \times 10^{10} sec^{-1}$.

Dedicatoria

Quisiera dedicar este trabajo a mi querida esposa Carol, a mi amado hijo Eduardo André, quienes fueron las personas que más se sacrificaron para que yo pudiera completar esta fase de mi vida. Sin ellos, este trabajo no tendría ningún sentido. También quiero dedicarlo a mis padres, pues fueron ellos los que me enseñaron todo lo verdaderamente importante en la vida.

Acknowledgments

There are a lot of people to which I have to be thankful for their involvement in this project. First, I would like to thank Dr. Angel López for his support and guidance during all these years of hard work. Special thanks goes to Dr. Héctor Méndez and Dr. Pat Rapp who were always there to answer any question that I had during this process, but who also offered me something more than knowledge, their friendship. To the guys working with me in the laboratory, Alexis, Carlos, Hector, Hugo, Jose, Kennie and Mauricio, we had a great time together and I learned a lot from them. To Sandra Troche, who was always making sure that everything was right so we can keep working.

I would also like to thank all the people and institutions that make this experiment possible. Being part of the FOCUS collaborations has been a great experience for me. Through all these people I learned what is real science.

To all of you, **Thanks.**

Contents

List of Tables

List of Figures

List of Abbreviations

BeO:	Beryllium Oxide.
BR:	Branching Ratio.
CERN:	Organisation Européenne pour la Recherche Nucléaire.
CITADL:	Čerenkov Identification Through A Digital Likelihood.
CKM Matrix:	Cabibbo-Kobayashi-Maskawa Quark-Mixing Matrix.
CP Violation:	Charge-Parity Violation.
CL:	Confidence Level.
CLP:	Primary Vertex CL.
CLS:	Secondary Vertex CL.
E687:	Fermilab Experiment 687.
E831:	Fermilab Experiment 831.
E791:	Fermilab Experiment 791.
Fermilab:	Fermi National Accelerator Laboratory.
FOCUS:	Fotoproduction Of Charm with an Upgraded Spectrometer.
GeV:	Giga Electron Volt.
IMU:	Inner Muon System.
CL_{imu}:	Inner Muon CL.
ISO_{prim}:	Primary Vertex Isolation.
ISO_{sec}:	Secondary Vertex Isolation.
L/σ:	Separation between the production and decay vertices divided by the error, σ, on that measurement.
MeV:	Mega Electron Volt.
MisID:	Percent of events misidentified within any specific analysis.
MISSPL:	Number of Missed Muon Planes.
M1:	Magnet Number 1.

M2:	Magnet Number 2.
OMU:	Outer Muon System.
CL_{omu}:	Outer Muon CL.
PAW:	Physics Analysis Workstation.
Pass1:	Basic event reconstruction stage.
PWC:	Proportional Wire Chambers.
Skim1:	First data reconstruction selection stage.
Skim2:	Second data reconstruction selection stage.
Skim3:	Third data reconstruction selection stage.
SSD:	Silicon Microvertex Detectors.
ZVPRIM:	Primary Vertex *z* Position.
ZVSEC:	Secondary Vertex *z* position.
Δ W(πK):	Kaonicity.
π_{con}:	Pion Consisitency.
Δ W($K\pi$):	Pionicity.

Chapter 1

Introduction

1.1 Objectives

The FOCUS experiment is probably the last fixed target experiment whose main goal is the study of *charm* particles. The available data give us the opportunity to study with great precision a wide range of physical processes (from lifetime measurements to CPT invariance tests) that can probe the Standard Model of Particle Physics. The large sample of reconstructed charm particles compared to previous experiments guarantees that results from FOCUS will be among the most accurate for charm decays.

The scope of this thesis is to present new measurements of the charm semileptonic branching ratios for the vector meson decays $D^+ \rightarrow \overline{K^{*0}}\mu^+\nu$ and $D^+ \rightarrow \rho^0\mu^+\nu$. These measurements can test different theoretical models that predict semileptonic *Form Factors* which will result in a better understanding of the CKM matrix elements and other parameters in the *charm* and *bottom* sector.

This thesis is organized as follows: Chapter 1 gives a brief description of the Standard Model of Particle Physics and the theory behind semileptonic decays. Chapter 2 gives a

summary of the results obtained by previous experiments. Chapter 3 describes the FOCUS spectrometer used to collect the data, with emphasis given to the most relevant components for this work. Chapter 4 presents the methodology used in the data selection process as well as the analysis technique employed in obtaining these results. Finally in the last two chapters the results are presented and compared not only to previous experimental results, but also with predictions made by theoretical models for semileptonic decays.

1.2 Theoretical Background

1.2.1 The Standard Model of Particle Physics

Particle Physics is the study of the fundamental constituents of matter. In a sense, Particle Physics is also the study of the early universe since the energies involved in this field were only naturally available during the first stages of the Big Bang.

The Standard Model of particle physics is a very successful phenomenological model that describes the elementary particles of matter and their interactions. By elementary we mean particles that are structureless and indivisible (at least at the scale of 10^{-16} cm). In the Standard Model particles are classified in two groups: *fermions* and *bosons*. The model also includes three of the four fundamental forces in nature. These forces are:

- The Electromagnetic Force
- The Weak Force
- The Strong Force

There is a great deal of effort to introduce into the Standard Model the gravitational force, but so far, nobody has been able to successfully do so. Fortunately, the mass scales involved in particle physics are so small that gravity has a negligible effect.

Fermions

The *fermions* are half spin particles that constitute the matter. They are classified as *quarks* and *leptons*. Both types of particles come in three generations. Individual quarks have fractional charge of $+2/3e$ or $-1/3e$ (where e is the magnitude of the electron charge) while their bound states always carry integer charge.

Charge	1^{st}generation	2^{nd}generation	3^{rd}generation
q = +2/3e	up (u)	charm (c)	top (t)
q = -1/3e	down (d)	strange (s)	bottom (b)

Table 1.1: Quarks

Charge	1^{st}generation	2^{nd}generation	3^{rd}generation
q = -1	electron (e)	muon (μ)	tau (τ)
q = 0	electron neutrino (ν_e)	muon neutrino (ν_μ)	tau neutrino (ν_τ)

Table 1.2: Leptons

Tables 1.1 and 1.2 show all twelve fermions. It is important to note that every particle has its own antiparticle. These antiparticles have the same mass as the particles but all their quantum numbers are reversed. All the visible mass in the universe is made of only two of these quarks and one lepton.[1] The *up* and *down* quarks make the protons and neutrons while the electron completes the atom that matter is made of.

The quarks cannot be found isolated in nature (this is known as confinement). They either form baryons (qqq or $\overline{qqq}$) or mesons($q\overline{q}$). Protons (uud) and neutrons (udd) are examples of baryons. As one moves from generation to generation the masses of the quarks increase. Determination of the mass of individual quarks is not trivial since the strong force that keeps them together contributes energy to the system and therefore mass.

Quarks not only carry electrical charge, but they also carry *color* charge. The color charge can be either *red*, *green* or *blue*. Only *colorless* combinations of baryons and

[1] This only constitutes $\sim$ 4 % of all the mass in the universe. The rest is composed of *Dark Matter* and *Dark Energy*. Dark matter is probably made of mass which is unknown today.

mesons are allowed. This new degree of freedom was introduced in order to account for the $\Delta^{++}(uuu)$ baryon. Baryons, as spin 1/2 particles, obey Pauli's exclusion principle that states that two identical particles cannot be in the same state with the same quantum numbers. In the case of the Δ^{++} we have three *u* quarks in the same level. This is resolved if the new quantum number *color* is introduced. Although this seems somehow arbitrary, the existence of the three colors has been established experimentally.

In contrast to quarks, leptons do not bind together to form particles. In the Standard Model, the neutrinos are massless, but recent experimental results have demonstrated that neutrinos can mix (change from one flavor to another) which implies that neutrinos do have a very small mass (See for example [1]). The main difference between leptons of different generations are their masses. Again as in the case for the quarks, as one moves from one generation to the other, the mass of the leptons increases.

Bosons

The *bosons* are integer spin particles that act as the forces intermediaries. Table 1.3 shows the four fundamental forces and their corresponding bosons [2].

Force	Boson	Spin/parity	Relative Strength	Mass (GeV)
Strong	gluon (G)	1^-	1	0
Electromagnetic	photon (γ)	1^-	10^{-2}	0
Weak	W^{+-}, Z^0	1^-,1^+	10^{-7}	80.42, 91.19
Gravity	graviton (g)	2^+	10^{-39}	0

Table 1.3: Force Intermediaries

The *Strong* force is responsible not only for keeping quarks forming baryons and mesons, but also for keeping the neutrons and protons inside the atomic nuclei. This force is mediated by the massless gluons. There are eight different gluons since they, as quarks,

[2]The graviton g is still a theoretical prediction that has never been observed but searches are currently undergoing.

carry color charge. The consequence of this is that gluons can interact not only with quarks, but also with other gluons.

Two interesting features about the strong interaction are its range and the confinement effect. The range of an interaction is inversely proportional to its gauge boson mass, so for a massless boson one would expect, as is the case for the photon, that the range of the strong interaction should be infinite. In fact just outside the atomic nuclei, this force becomes so weak that the electromagnetic force takes over.

Confinement is the explanation for the fact that we can not see free quarks in nature. The potential for the strong force interaction can be written as [2]:

$$\mathbf{V_s} = -\frac{\mathbf{4}}{\mathbf{3}}\frac{\alpha_\mathbf{s}}{\mathbf{r}} + \mathbf{kr} \tag{1.1}$$

The first term in equation 1.1 dominates at small r, while the second term is responsible for confinement. This have the effect that when one wants to free quarks, $q\overline{q}$ pairs are formed since the energy needed to separate the quarks is greater than the energy to form new $q\overline{q}$ pairs.

The *Electromagnetic* force is responsible for keeping the atoms together and along with the gravitational force dominates our everyday live. It is mediated by the massless photon and has infinite range.

The *Weak* force mediated by the massive $W^{\pm}$ and Z^0 is responsible for the decay of quarks within and across generations (flavor changing), and decays of lepton within the same generation. Since the mass of the gauge boson is so heavy, the weak interaction has a range of about 10^{-16} cm.

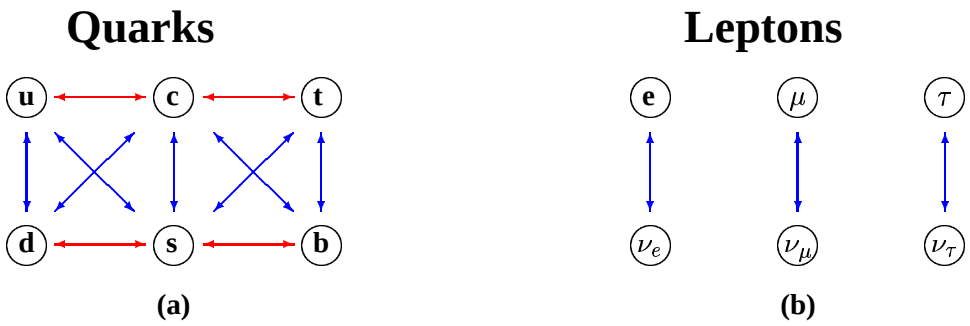

Figure 1.1: Weak decay transitions. The weak force change the flavor of the quarks either within their same generation or across generations, whereas in the case of leptons, they can only decay within their same generation.

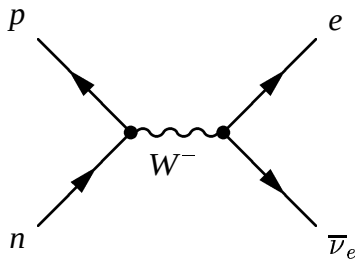

Figure 1.2: Feynman Diagram for Beta decay

The first known weak interaction was the β-decay. In this process a neutron ($u\ d\ d$) decays into a proton ($u\ u\ d$), electron and an electron neutrino.

$$\mathbf{n} \rightarrow \mathbf{p} + \mathbf{e}^- + \overline{\nu}_\mathbf{e} \tag{1.2}$$

In terms of quarks, one of the d quarks of the neutron decays into a u quark through a W which then decays into an electron and electron neutrino.

1.2.2 Quark Mixing Matrix (CKM)

Quark generations are in separate doublets:

$$\begin{pmatrix} u \\ d \end{pmatrix}, \quad \begin{pmatrix} c \\ s \end{pmatrix}, \quad \begin{pmatrix} t \\ b \end{pmatrix} \tag{1.3}$$

The transitions of quarks between and across generations and the probabilities for those events to occur is more easily understood with the Cabibbo-Kobayashi-Maskawa (CKM) matrix [3]. The CKM matrix is a 3×3 unitary matrix that relates the mass eigenstates d, s, b to the weak eigenstates d', s' and b'.

$$\begin{pmatrix} d' \\ s' \\ b' \end{pmatrix} = \begin{pmatrix} V_{ud} & V_{us} & V_{ub} \\ V_{cd} & V_{cs} & V_{cb} \\ V_{td} & V_{ts} & V_{tb} \end{pmatrix} \begin{pmatrix} d \\ s \\ b \end{pmatrix} \tag{1.4}$$

Within this framework, the probability for the transition $c \rightarrow s$ is proportional to $|V_{cs}|^2$. It is important to note that the elements that lie in the diagonal are very close to unity and represent the transitions within the same generation. These *Cabbibo favored* transitions are approximately equal to $cos\theta_c$, where $\theta_c \approx 12^\circ$ is the Cabbibo angle. The near off-diagonal elements of the matrix are proportional to $sin\theta_c$. These transitions are called *Cabbibo suppressed* and represent transitions across generations. The far off-diagonal elements have an additional phase angle that is related to weak decays which do not conserve Charge-Parity.

1.2.3 Semileptonic Decays

Semileptonic decays are processes where we have leptons along with hadrons (either mesons or baryons) in the final state. These decays offer two main advantages for the study of hadronic currents that are of great importance:

- Semileptonic decays can only proceed through the spectator model.
- The matrix element can be parameterized into a well understood leptonic current and a hadronic current.

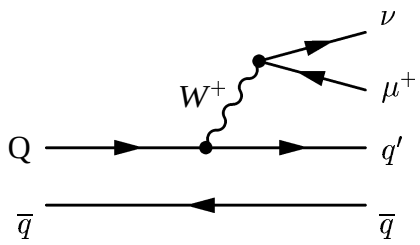

Figure 1.3: Spectator diagram for semileptonic decay $P_{Q\overline{q}} \rightarrow X_{q'\overline{q}}\mu^+\nu$

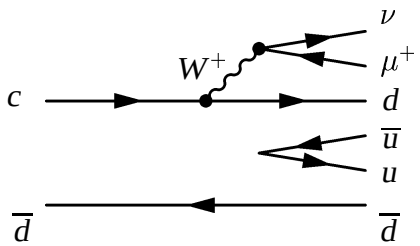

Figure 1.4: Spectator diagram for semileptonic decay $D^+ \rightarrow \rho^0\mu^+\nu$

Figure 1.3 shows the semileptonic transition for $P_{Q\overline{q}} \rightarrow X_{q'\overline{q}}\mu^+\nu$. These Feynman diagrams are known as spectator diagrams because the only quark that takes part of the interaction is $Q \rightarrow q'W^+$ while the $\overline{q}$ remains as a *spectator* in the process. Figure 1.4

shows the spectator diagram for the decay $D^+ \to \rho^0 \mu^+ \nu$. During this process, the quark decay is $c \to dW^+$. An important feature about this process is that a $u\overline{u}$ pair is created from the vacuum. Each of these quarks from the vacuum couples with the spectator $\overline{d}$ and with the d quark to form the two pions to which the ρ^0 decays instantly. The diagram for the $D^+ \to \overline{K^{*0}} \mu^+ \nu$ decay is the same as this one but now the quark decay is $c \to sW^+$. The $\overline{K^{*0}}$ decays to $K^-\pi^+$. In this case, the s quark couples with the $\overline{u}$ quark to form a Kaon while the spectator $\overline{d}$ quark couples with the remaining u quark from the $u\overline{u}$ pair. In $D^- \to K^{*0}\mu^-\nu$, the K^{*0} decays to $K^+\pi^-$. Therefore the muon and the Kaon always have opposite charge in these decays.

The amplitude for the semileptonic decay $P_{Q\overline{q}} \to X_{q'\overline{q}} l^- \overline{\nu}$ can be written as follows [4]:

$$\mathcal{M}(P_{Q\overline{q}} \to X_{q'\overline{q}} l\nu) = -i\frac{G_F}{\sqrt{2}} V_{q'Q} L^\mu H_\mu \tag{1.5}$$

where the leptonic and hadronic currents are:

$$L^\mu = \overline{u}_l \gamma^\mu (1-\gamma_5) v_\nu \tag{1.6}$$

$$H_\mu = < X|\overline{q}'\gamma_\mu(1-\gamma_5)Q|P > \tag{1.7}$$

The effects of the hadronic current can be related to the semileptonic *Form Factors*. The form factors are Lorentz invariant functions of q^2, the square of the momentum transfer between the parent meson and the daughter vector. For the decay $P_{Q\overline{q}} \to X_{q'\overline{q}} l^- \overline{\nu}$ of a pseudo-scalar meson decaying into a vector meson, we need four form factors to fully describe the hadronic current. Although for this work we did not measure the form factors, such measurements are still one important goal for the FOCUS collaboration.

For such semileptonic decays,

$$q^2 = (\mathbf{p} - \mathbf{x})^\mathbf{2} = \mathbf{M_W^2} * \tag{1.8}$$

where $\mathbf{p}$ is the four momentum of the parent pseudo-scalar, $\mathbf{x}$ is the four momentum of the vector meson and M_W* is the mass of the virtual W exchanged during the interaction.

Interactions with high q^2 are more favorable for the production of low mass mesons since the virtual W along with the daughter meson takes most of the available energy [5]. This is also called the *zero-recoil* configuration since the daughter quark receives little or no momentum kick. Although the $q^2 = 0$ configuration is the least favorable for meson production, it is at this kinematic point ($q^2 = 0$) that theory is able to make the most precise predictions about the decay rates.

It has been demonstrated by O'Donnell and Turan [6] that at the limit of vanishing lepton mass and $q^2 = 0$, the differential decay rates for a $D \to Vl\nu$, where the vector can be either $\overline{K^{*0}}$ or a ρ^0 is determined by only one form factor, A_0. This decay rate becomes:

$$\left.\frac{d\Gamma(D \to Vl\nu)}{dq^2}\right|_{q^2\to 0} = \frac{G_F^2}{192\pi^3 m_D^3}|V_{cQ}|^2(m_D^2 - m_V^2)^3|A_0^{D\to V}(0)|^2 \tag{1.9}$$

Following this approach, the ratio for the differential decay rate for $D^+ \to \rho^0\mu^+\nu$ and $D^+ \to \overline{K^{*0}}\mu^+\nu$, can be expressed as:

$$\frac{[d\Gamma(D^+ \to \rho^0\mu^+\nu)/dq^2]_{q^2\to 0}}{\left[d\Gamma(D^+ \to \overline{K^{*0}}\mu^+\nu)/dq^2\right]_{q^2\to 0}} = \frac{|V_{cd}|^2}{|V_{cs}|^2}\left(\frac{m_D^2 - m_\rho^2}{m_D^2 - m_{\overline{K^{*0}}}^2}\right)^3 \frac{|A_0^{D\to\rho}(0)|}{|A_0^{D\to\overline{K^{*0}}}(0)|} \tag{1.10}$$

Chapter 2

Previous Work

2.1 Observations of $D^+ \to \overline{K^{*0}}\mu^+\nu$ and $D^+ \to \rho^0\mu^+\nu$

The most important work in the decay channels that we studied was carried out by experiments E653, E687 (FOCUS predecessor) and E791.

2.1.1 E687

The E687 collaboration collected data during the 1987-88 and 1990-91 fixed target run in Fermilab Wideband Photon Beam. The E687 experiment [7] studied high energy photon-beryllium interactions using a multi-particle magnetic spectrometer with excellent particle identification, vertex measurement and calorimeter capabilities. The average photon energy was ~ 220 GeV. The charged products of charm decays were tracked using twelve planes of silicon micro-strips and twenty planes of proportional wire chambers (PWC's). The particle momentum was determined from the track bending in the field of two large magnets working in opposite polarities. Identification of charged hadrons was done by a system of three Čerenkov detectors operating in threshold mode to discriminate

between pions and kaons from 4.5 to 61 GeV. The muons were identified in the inner muon detector that was placed in the downstream end of the spectrometer and was shielded by the upstream detectors and two blocks of steel.

Among the semileptonic channels that E687 studied were $D^+ \to \overline{K^{*0}}\mu^+\nu$ [8] and $D^+ \to \rho^0\mu^+\nu$ [9]. For the decay mode $D^+ \to \overline{K^{*0}}\mu^+\nu$, E687 searched for a $K\pi\mu$ combination that formed a secondary vertex with a CL greater than 10 % . It was required that the primary vertex and secondary vertex were separated by L/σ greater than 20. This cut was used to eliminate contamination from non-charm backgrounds. The primary vertex was found after all tracks in the secondary vertex were eliminated from the search. It was also required that the secondary vertex was isolated from other tracks in the event (not including those coming from the primary). Combinations in which the muon and the kaon had the same sign are called *Wrong Sign (WS)*. This WS was used to model the remaining background since this charge combination is only possible if the two particles are not coming from the same vertex.

To normalize the sample E687 used the decay mode $D^+ \to K^-\pi^+\pi^+$. This decay was chosen because of the similarity with $D^+ \to \overline{K^{*0}}\mu^+\nu$ events. All $D^+ \to K^-\pi^+\pi^+$ events were selected with exactly the same criteria as for $D^+ \to \overline{K^{*0}}\mu^+\nu$ events except for the identification cuts. This had the advantage that most systematic errors cancel when the branching ratio was taken.

E687 reconstructed 875 events and measured the branching ratio $\frac{\Gamma(D^+\to\overline{K^{*0}}\mu^+\nu)}{\Gamma(D^+\to K^-\pi^+\pi^+)} = 0.56 \pm 0.04 \pm 0.06$. They also measured the form factors that governed this decay to be: $R_v = 1.74 \pm 0.27 \pm 0.28$, $R_2 = 0.78 \pm 0.18 \pm 0.10$. The fit for the form factors was done after calculating the kinematic variables associated with the events and using the matrix element form and methodology described in ref [10].

As mentioned before, E687 also measured the Cabbibo suppressed decay

$D^+ \to \rho^0\mu^+\nu$. This is far more difficult to study than $D^+ \to \overline{K^{*0}}\mu^+\nu$ since there are many semileptonic decays with two pions in the final state that contribute to the background.

To select the sample, E687 required a secondary vertex with a $\pi\pi\mu$ combination in the final state with a Cl greater than 1%. The L/σ cut was required to be greater than 20 in order to suppress non-charm background. To reduce contamination from other two-pion final-state modes, the invariant mass for the $\pi\pi\mu$ combination was required to be between 1.22 and 1.8 GeV/c^2. The data was fitted using a binned maximum likelihood with contributions from the signal term ($D^+ \to \rho^0\mu^+\nu$) and several semileptonic decay backgrounds whose shape was given by Monte Carlo simulation. The normalization was done using the decay mode $D^+ \to \overline{K^{*0}}\mu^+\nu$ in order to cancel most systematics errors. Again, as in the case for the $D^+ \to \overline{K^{*0}}\mu^+\nu$ analysis, the selection for $D^+ \to \rho^0\mu^+\nu$ and $D^+ \to \overline{K^{*0}}\mu^+\nu$ was done in a similar way with the exception of the identification cuts. Their result for the branching ratio was: $\frac{\Gamma(D^+\to\rho^0\mu^+\nu)}{\Gamma(D^+\to\overline{K^{*0}}\mu^+\nu)} = 0.079 \pm 0.019$

2.1.2 E653

Fermilab Experiment E653 measured $D^+ \to \overline{K^{*0}}\mu^+\nu$ form factors [11] and branching ratio [12]. In this experiment a 600 GeV/c π^- beam was incident on a long emulsion target. The upstream spectrometer consisted of 18 planes of silicon micro-strips followed by a wide aperture dipole magnet. The downstream spectrometer consisted of a muon detector with 12 drift chamber planes on each side of a toroidal iron magnet.

To make the event selection, they required a three body secondary vertex outside the target with $L/\sigma > 14$. The hadron momentum had to be larger than 8, 8 and 3 for the kaon, muon and pion respectively. Since this analysis did not use any hadron identification, the K mass was assigned to the track with the opposite sign as the D, while the π mass was assigned to the remaining track. Background from neutral hadrons was reduced by

requiring $1.6 \leq M_{min} \leq 1.97\ GeV/c^2$ with M_{min} defined as:

$$M_{min} = \sqrt{m_{vis}^2 + p_t^2} + \sqrt{m_\nu^2 + p_t^2} \tag{2.1}$$

where m_{vis} is the visible mass (mass of the charged particles) and p_t is the transverse momentum and the neutrino mass $m_\nu = 0$. Finally, events with $0.83 \leq M_{K\pi} \leq 0.95$ were selected.

E653 reconstructed 305 events and measured $\frac{\Gamma(D^+\to\overline{K^{*0}}\mu^+\nu)}{\Gamma(D^+\to K^-\pi^+\pi^+)} = 0.46 \pm 0.07 \pm 0.08$ Their fitted form factors were: $R_v = 2.00^{+0.34}_{-0.32} \pm 0.16$ and $R_2 = 0.82^{+0.22}_{-0.23} \pm 0.11$

2.1.3 E791

Fermilab experiment E791 measured both $D^+ \to \overline{K^{*0}}\mu^+\nu$ form factor [13] and $\frac{\Gamma(D^+\to\rho^0\mu^+\nu)}{\Gamma(D^+\to\overline{K^{*0}}\mu^+\nu)}$ [14]. E791 was a fixed target hadroproduction with a 500 GeV/c π^- beam. There were 23 planes of silicon micro-strips and 45 drift chamber planes and proportional wire chambers that were in charge of the tracking. The hadrons were identified with two multi cell Čerenkov that could discriminate pions from kaons in the momentum range from 6-36 GeV/c. The muon detector was a plane of scintillator strips shielded by 2.4 m of iron.

The selection criteria for $D^+ \to \overline{K^{*0}}\mu^+\nu$ events was: three track secondary vertex with the tracks identified as a kaon, a pion and a muon. The two hadrons had opposite charge. Right Sign (RS) events were those where the muon and the kaon had opposite charge sign, while kaons and muons with the same charge were assigned to the Wrong Sign sample. This Wrong Sign was used to model the background. To reduce background from muon misidentification, the pion momentum had to be larger than 8 GeV. Background from $D^+ \to K^-\pi^+\pi^+$ was reduced by calculating the D invariant mass with the three tracks and requiring that this mass be less than that of the D. E791, as E653, used a cut in

M_{min}. Their cut was: $1.6 \leq M_{min} \leq 2.0\ GeV/c^2$. Events with $0.85 \leq M_{K\pi} \leq 0.94$ were retained, yielding a final data sample of 3629 RS and 595 WS events.

The Form Factors were extracted using an unbinned maximum likelihood fitting technique. This fit was done after calculating all four kinematic variables: $\cos\Theta_v$, $\cos\Theta_l$, q^2 and χ. Their results were: $R_v = 1.90 \pm 0.11$, $R_2 = 0.72 \pm 0.81$. They also made the first measurement of R_3: $R_3 = -0.25 \pm 0.34$.

For the decay mode $D^+ \to \rho^0 l^+\nu$, E791 required a secondary vertex with two hadrons and a lepton in the final state with unit charge. After the lepton was identified, the two remaining tracks were assigned pion masses. To reduce contamination from pions decaying in flight, the muon candidate was required to have a momentum larger than 12 GeV/c. At this momentum range, E791 probability for misidentified hadrons as muons was less than 1.6 %. Hadron momentum had to be greater than 6 GeV/c. For the secondary vertex, L/σ had to be larger than 20 and the vertex was required to be outside the material by about $5\sigma_m$, where σ_m is the error on the measured separation.

To reduce background from non charm final states, E791 demanded a cut in M^2_{miss}. This cut was: $-0.10 \leq M^2_{mis} \leq 0.15$, where

$$M^2_{miss} = M^2_D + M^2_{vis} - 2M_D\sqrt{M^2_{vis} + p^2_t} \tag{2.2}$$

$D^+ \to \overline{K^{*0}} l^+\nu_l$ events were reduced by three additional requirements. Čerenkov information was used to reject about 51% of $D^+ \to \overline{K^{*0}} l^+\nu_l$ while retaining 92% of $\pi\pi$ pairs. The $M_{min}(K\pi l\nu_l)$ was calculated and required to be greater than 2.00 GeV/c, and the $K\pi$ invariant mass that were between 0.85 and 0.93 were rejected.

For the final results, only events with $M(\pi\pi)$ between 0.65 and 0.90 were used. This cut helped eliminate contributions from $D^+_s \to \eta\mu\nu$ and $D^+ \to \eta\mu\nu$. Feed-through from other $\pi\pi$ final states were estimated using Monte Carlo efficiencies from PDG (1994)

branching fractions for these decays. E791 used same sign pions to model combinatoric background. This background was identified as Wrong Sign.

The fit was done using a binned maximum likelihood function. This function was a p-wave Breit Wigner + F(M), a function representing the WS distribution.

$$F(M) = N_0(M - m_0)^\alpha \times \exp[c_1(M - m_0) + c_2(M - m_0)^2] \tag{2.3}$$

where $N_0, M, c_1 and c_2$ were the parameters to be fitted.

After background subtraction, E791 reported a yield of 54 ± 18 events for $D^+ \to \rho^0\mu^+\nu$ and 49 ± 17 events for $D^+ \to \rho^0 e^+\nu$. Their measured branching ratios were: $\frac{\Gamma(D^+\to\rho^0\mu^+\nu)}{\Gamma(D^+\to\overline{K^{*0}}\mu^+\nu)} = (5.1 \pm 1.5 \pm 0.9)\%$ and $\frac{BR(D^+\to\rho^0 e^+\nu)}{BR(D^+\to\overline{K^{*0}}e^+\nu_l)} = (4.5 \pm 1.4 \pm 0.9)\%$. Combining these results, E791 calculate $\frac{BR(D^+\to\rho^0 l^+\nu)}{BR(D^+\to\overline{K^{*0}}l^+\nu_l)} = (4.7 \pm 1.3)\%$.

2.1.4 CLEO Collaboration

The most recent measurement of the $D^+ \to \overline{K^{*0}}l^+\nu$ branching ratio was done by the CLEO Collaboration [15]. For this measurement, the CLEO collaboration used $13.53fb^{-1}$ of the data collected at Cornell Electron Storage Ring. $9.13fb^{-1}$ of the total luminosity was on the $\Upsilon(4s)$ resonance, while the remaining $4.40fb^{-1}$ luminosity was below the $B\overline{B}$ threshold.

In this analysis, the decay chain studied was $D^{*+} \to D^+\pi^0, D^+ \to \overline{K^{*0}}l^+\nu$. The muon candidate was required to have penetrated 5 interaction lengths in the muon detector with a muon momentum greater than $1.4GeV/c$ for $|\cos\theta| \leq 0.61$ or greater than $1.9GeV/c$ for $0.61 \leq |\cos\theta| \leq 0.81$, where θ is the polar angle between the e^+e^- axis and the momentum of the particle. The π^0 were selected from $\gamma\gamma$ pairs for which $|M_{\gamma\gamma} - M_{\pi^0}| < 2.5\sigma$, where σ is the standard deviation of the π^0 mass. For the neutrino momentum reconstruction, the CLEO Collaboration used two different methods

which yielded three momentum solutions. In the first method, it was assumed that the thrust direction was the direction of the D. In this case the momentum of the charged particles and the constrained that $M_{K\pi l\nu} = M_D$ provided ans ellipsoid of allowed D momentum. The two intersections between the ellipsoid and the D direction were chosen. The difference between these D momentum and the momentum of the charged particles was then used as the neutrino momentum.

In the second method, the missing momentum of each event was used as an estimate for the neutrino momentum. Of the three solutions, the one with $\delta_m = M_{K\pi l\nu\pi^0} - M_{K\pi l\nu}$ closest to the known value of $M_{D^{*0}} - M_{D^+}$ was chosen.

The number of events was extracted after fitting both $M_{K\pi}$ and δ_m. The data was divided in 50 bins of δ_m (25 bins for muon mode) and the $M_{K\pi}$ was plotted for each bin. For each bin, the number of events was extracted. The yields were then plotted as a function of δ_m and the number of signal events was obtained with another fit.

The CLEO Collaboration reported $R_e^+ = \frac{BR(D^+\to\overline{K^{*0}}e^+\nu)}{BR(D^+\to K^-\pi^+\pi^+)} = 0.74 \pm 0.04 \pm 0.05$, $R_\mu^+ = \frac{BR(D^+\to\overline{K^{*0}}\mu^+\nu)}{BR(D^+\to K^-\pi^+\pi^+)} = 0.72 \pm 0.10 \pm 0.06$ and $R_l^+ = \frac{BR(D^+\to\overline{K^{*0}}l^+\nu)}{BR(D^+\to K^-\pi^+\pi^+)} = 0.74 \pm 0.04 \pm 0.05$. Using these values and E791 measured form factors, CLEO also calculated $A_1(0) = 0.69 \pm 0.07, A_2(0) = 0.48 \pm 0.08,$ and $V(0) = 1.25 \pm 0.15$.

Chapter 3

FOCUS Experimental Setup

Everything that we see in our everyday life is made of protons(uud), neutrons(udd) and electrons. All these particles that compose the atoms belong to the first family of quarks and leptons. Since all other particles are too heavy to be produced naturally, we need to produce them in the laboratory to be able to study them. There are two ways to create particles: either in a *fixed target* experiment in which a high energy beam interacts with a stationary target to produce heavy particles or in a *collider experiment* in which two high energy beams collide head on to produce the interactions. Once the particles are created, we need to identify the products of the interactions. The identification process consist of the determination of the mass and charge of the particles.

E831, also known as FOCUS (*Fotoproduction Of Charm with an Upgraded Spectrometer*), was a fixed target experiment that collected data during the 1996-1997 Fermilab fixed target run. Interactions studied by FOCUS were created when a high energy photon beam impinged upon a BeO target.

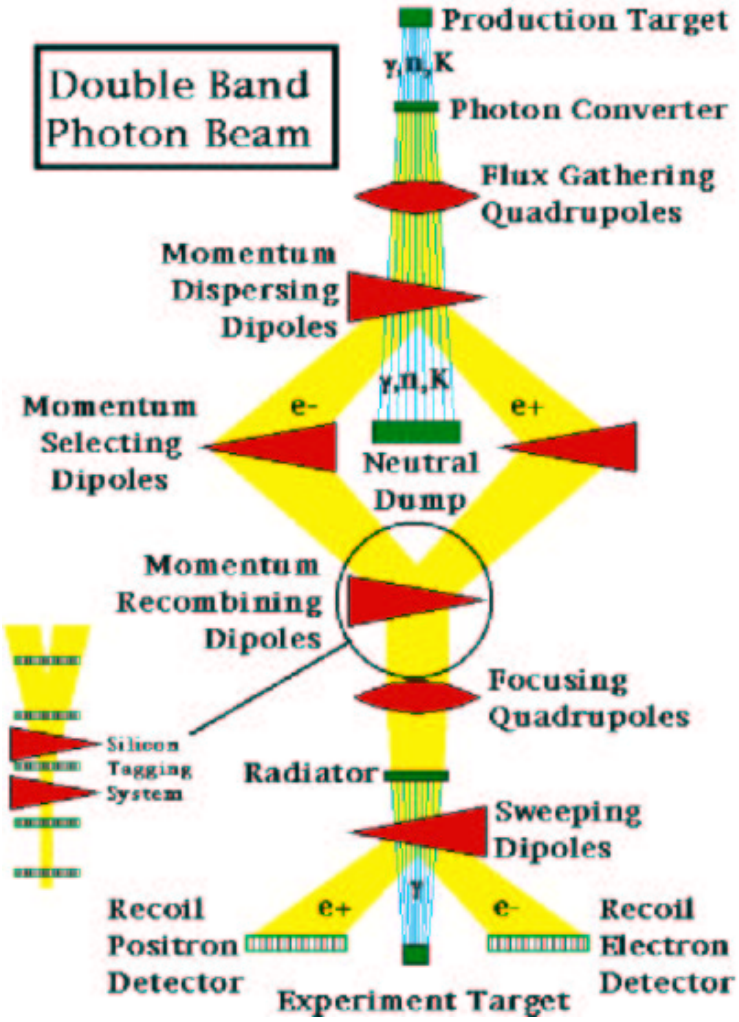

Figure 3.1: Schematic drawing showing the process to produce the beam used in FOCUS

3.1 FOCUS Beam

The photon beam used by FOCUS was obtained from protons delivered by the Tevatron after a process involving three steps. In the first stage, protons coming from the Tevatron with an energy of 800 GeV interacted with a cooled liquid deuterium target. From this interaction, hadronic secondaries were produced and the charged particles were swept out by magnets. Photons from the decays of π^0 and η's then struck the photon

converter and produced e^-e^+ pairs. The electron pair was then focused using quadrupole magnets and bent around a neutral dump that absorbed the non-interacting neutral particles. At this moment, the beam momentum was selected to be ~ 250 GeV with the use of collimators. In this stage, the electrons and positrons were traveling along different paths and then recombined into a single beam by the momentum recombining dipoles. This beam was focused with focusing quadrupoles and then interacted with a radiator which produced photons by the bremsstrahlung process. After this interaction, the remaining electrons were swept away using sweeping dipoles leaving only a clean photon beam to interact with the experimental target. The average energy of these photons was ~ 180 GeV. A schematic drawing of the FOCUS beamline is shown in Figure 3.1.

3.2 Experimental Target

FOCUS used a BeO target for charm production. The choice of material was done taking into consideration the idea of producing as much charm hadronic interactions as possible while suppressing the number of e^+e^- pairs. The pair production depends on Z^2, Z being the atomic number, while the hadronic production depends on A, where A is the atomic weight. BeO, having a high A/Z ratio, made it a good target material for clean charm production. Another advantage of BeO is its high density. This allowed to segment the target and enhance the number of secondaries occurring outside the target material. Studies from E687 showed that events having the secondary vertex outside the target were cleaner than those with the secondary inside the target. The problem with secondaries inside the material is that multiple interactions can “fake” detached vertices creating hard to model backgrounds [16].

Figure 3.2: FOCUS Target. Schematic diagram showing the target configuration including the embedded TSSD's and SSD's

3.3 FOCUS Spectrometer

The FOCUS spectrometer was a two magnet spectrometer with excellent vertex resolution and particle identification. It was designed to measure the interactions of high energy photons with a BeO target. The spectrometer was an upgrade of the spectrometer used by E687 in which many of the detectors and reconstruction algorithms were improved. In the following sections, I will give a brief description of the main detectors used in the spectrometer. A complete and detailed description can be found in the references following each detector. Figure 3.3 shows a schematic diagram of the FOCUS spectrometer.

3.3.1 Tracking Systems

The tracking of the charged particles coming out of the target was done with the use of the target silicon strip detectors (TSSD), silicon strip detectors (SSD) and proportional

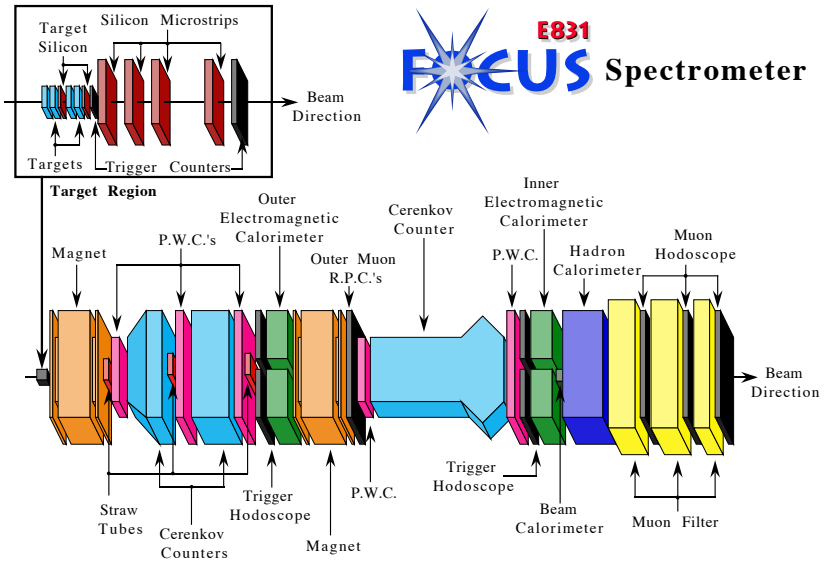

Figure 3.3: FOCUS Spectrometer. Schematic diagram of the spectrometer. The insert shows the target region.

wire chambers (PWC's). Since FOCUS used a segmented target to increase secondary vertices outside the material, the TSSD were interleaved between the target segments. This arrangement of detectors allows for a more accurate vertex resolution. The SSD's were arranged in four stations downstream of the last target segment and just before the first magnet M1. Downstream of M1, the tracking was done with the PWC's. There were five such stations (P0, P1, P2, P3, P4) throughout the spectrometer. Both magnets (M1 and M2) and the three Čerenkov counters were embedded with the PWC's. This allowed not only to have very accurate vertex information, but also a very good momentum resolution. Details of the target silicon detectors can be found in reference [17]

3.3.2 Particle Identification

Charged particle identification was done with three multi-cell threshold Čerenkov detectors. These three detectors were able to identify pions, kaons, electrons and protons.

Čerenkov radiation is emitted when a charged particle is traveling through a medium faster than the speed of light inside that medium (c/n):

$$\beta = \frac{p}{E} = \frac{p}{\sqrt{p^2 + m^2}} > \frac{1}{n} \tag{3.1}$$

where n is the index of refraction of the medium. The angle of the emitted light is described by

$$\cos\theta_c = \frac{1}{n\beta} \tag{3.2}$$

Čerenkov radiation will be emitted only when the momentum of a particle with mass m is greater than $p_{threshold}$ [18].

$$p_{threshold} = \frac{m}{\sqrt{n^2 - 1}} \tag{3.3}$$

In a threshold Čerenkov, the identification is based on whether or not a particle emits radiation. Since the momentum of the incoming particle is known, the mass can be inferred. The medium for each Čerenkov detector in FOCUS was carefully selected to be able to distinguish pions from kaons and protons in a wide momentum range. For a complete description of the Čerenkov systems in FOCUS and the identification algorithm, see reference [19].

Muon identification was done with two muon detectors. These were the Inner Muon System (IMU) and the Outer Muon System (OMU). The IMU system detected muons that passed through both magnets, while the OMU system detected less energetic muons that passed only through M1.

Since muons are very massive in comparison to the electron, they suffer very little energy loss and can penetrate large amounts of material whereas electrons and hadrons cannot do this. This is the basis for muon identification.

The IMU system consisted of three stations (MH1, MH2 and MH3) at the most downstream part of the spectrometer. Each station was shielded with steel to ensure

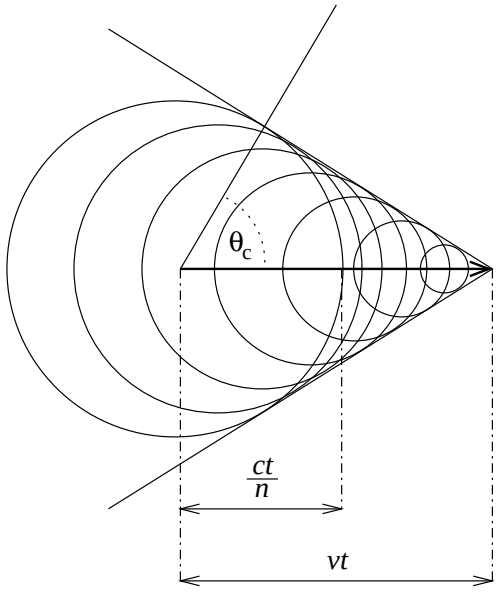

Figure 3.4: Čerenkov radiation wavefront. The figure shows the expanding spheres of radiation as the particle moves through the medium. The particle trajectory is to the right while the wavefront moves out.(Figure adapted from reference [20])

that only muons got to them. The OMU system was placed after M2 and the Outer Electromagnetic Calorimeter (OE). This system detected muons with large angles ($> 30mrad$). Both M2 and the OE worked as filters for the detector.

3.3.3 Analysis Magnets

The momentum of the charged particles in the spectrometer was determined with the use of two large aperture dipole magnets with opposite polarities (M1 and M2). If we can accurately know the trajectory before the magnet and the trajectory after the magnet, the momentum can be measured using [20]:

$$p_{\perp} = qB\rho \tag{3.4}$$

where ρ is the radius of curvature and q is the charge of the particle.

3.3.4 Calorimetry

The energy of the neutral particles was measured with three calorimeters, i.e. the Inner Electromagnetic Calorimeter (IE), the Outer Electromagnetic Calorimeter (OE) and the Hadronic Calorimeter (HC). Although in this work we did not use the information from the calorimeters, a brief description of the principles governing the determination of the energy of neutral particles with the use of calorimeters will be given in this section.

Electromagnetic calorimeters rely on bremsstrahlung and pair creation. In the most simple model, an electron with energy E_0 enters the calorimeter and after transversing one radiation length (X_0), it radiates a photon with half its energy ($E_0/2$). The radiated photon converts to an electron pair, each with half the photon energy ($E_0/4$), after it have traveled an additional radiation length. The original electron (now with energy ($E_0/2$), again radiates a photon. At this point, after two radiation length, we have two electrons, one positron and one photon. This process is called a shower. The electromagnetic shower reaches a maximum and then stops suddenly when the energy of the particles inside the shower falls bellow E_c, the energy needed for electrons to radiate through bremsstrahlung ($E_c \sim 100MeV$) [18].

The number of particles at the maximum is given by:

$$N_{max} = \frac{E_0}{E_c} \tag{3.5}$$

Using the above equation, the energy of the incident particle can be determined.

In contrast to the electromagnetic calorimeter shower which scale withe X_0, hadronic calorimeters scales with the nuclear absorption length (λ). In most materials $\lambda >> X_0$ which means that hadron showers are longer than electromagnetic showers. The main process for the the development of hadronic showers is a succession of inelastic hadronic

interactions which produces not only multiple particles, but also the emission of particles from nuclear decays of excited nuclei [21].

3.4 General Data Reconstruction

During the experimental run, FOCUS collected about 6000 tapes ($\approx$ 30 TB) containing information that came from the detectors (raw data). These were the signal recorded by each component of the spectrometer such as hits in the tracking systems, energy deposited in the calorimeters, hits in the muon detector, etc. This information by itself is useless for our purposes. It was necessary to reconstruct and classify each event that passed through the spectrometer in order to be able to look for the processes that we are interested. The reconstruction and classification of the events were done in three stages: *Pass One*, *Skim One*, *Skim Two*.

3.4.1 Pass One

During Pass One, all the information recorded on the tapes were converted into the physical quantities needed for all of the FOCUS analyzes. In this stage, for example, the tracks left by the passing of the charged particles through the tracking systems, were reconstructed from the hits on each individual plane. Also, quantities such as momentum, energy and charge were assign to each particle in the events. The reconstructed data was then written to another 6000 tapes set. This process took about a year to be completed.

3.4.2 Skim One

The main purpose of Skim One was to divide the Pass One data into smaller data sets of different physics topics. During this skim, very general selection criteria were applied.

The output of this process were six super-streams. Skim One took almost five months to be completed and was done at Vanderbilt University and the University of Colorado.

Super-stream	Description	Institution
1	Semileptonic	UPR Mayagüez
2	Global Vertex and K_s	U. of Illinois
3	EM and ϕ	Brazil, CPBF
4	Baryons	Fermilab
5	Diffractive, Leptonic and Out of Target	U. of California
6	SEZDEE	U. of California

Table 3.1: Skim 2 Super-streams

3.4.3 Skim Two

Skim Two was the last skim process applied to all the data collected during the FOCUS experiment. In this skim, each super-stream was divided into even smaller data sets, each of which contain events of a very specific process.

The Skim Two responsibility was shared among the institutions that form the FOCUS collaboration. The University of Puerto Rico was responsible for Super-stream 1 (SS1) which was divided into five sub-streams. Our data sample was taken from the Semimuonic sub-stream, while the normalization mode was taken from the Slepnrm sub-stream. Events in the Semimuonic sub-stream were those with at least one muon and either a kaon, a pion or a proton in the secondary vertex. The muon candidate was required to have muon CL greater than 0.05% and momentum greater than $4GeV$ for muons identified in the Outer Muon System or momentum greater than $8GeV$ for muons identified in the Inner Muon System. The pion candidates were required to have pionicity greater than 2 and the kaon candidates were required to have kaonicity greater than 1. The minimum separation between the primary and the secondary was 1.5σ.

SS1 Sub-stream	Description	Num. of Tapes
1	Semimuonic	26
2	Dileptonic and PPbar	45
3	Semielectronic with mesons	37
4	Semielectronic with baryons	27
5	Normalization (Slepnrm)	58

Table 3.2: SS1 sub-streams

Chapter 4

Methodology

In this chapter discuss all the methodology used in our studies. First, a brief description of some of the most important cuts used will be given, followed by the criteria used in the event selection and the fitting technique employed to extract the different yields for the Branching ratio calculations.

4.1 Cut Definitions

L/σ In charm fixed target experiments, L/σ is one of the most important cuts since particles containing charm travel in the spectrometer an average of 1.5 cm. This has the advantage that there is a significant separation between the production (primary) vertex and the decay (secondary) vertex. L/σ refers to this separation (L) divided by the uncertainty in the measurement (σ).

Confidence Level (CL) Variable used for hypothesis testing. If the hypothesis is correct, the CL is equally likely to have any value between 0 and 1 (flat distribution). If the

hypothesis is incorrect, then small values of CL (high values of χ^2) are obtained. Using this, it is possible to differentiate by requiring the CL greater than some value.

Primary Isolation (Iso1) This variable refers to the highest CL for the hypothesis that the tracks in the secondary vertex are really coming from the primary vertex. Iso1 is calculated after adding the tracks in the secondary vertex to the primary vertex one by one. Usually, this variable is required to be very small.

Secondary Isolation (Iso2) This is the highest CL for the hypothesis that any other track in the SSD also belongs to the secondary vertex. It is calculated for all remaining tracks in the SSD. As in the case for Iso1, Iso2 is required to be small.

Wobs Variable returned by CITADL [19]. There are four such variables, one for each particle hypothesis (Wobs(e), Wobs(p), Wobs(π) and Wobs(K)). The Wobs are the negative log likelihood for a given particle hypothesis.

Pion consistency (π_{con}) $Wobs(\pi) - Wobs(best)$. Used for pion identification. It is a comparison between the probability of the hypothesis that the track is a pion against the probability of the best hypothesis (lowest wobs). This variable will only take negative values or zero. Zero means that the most likely hypothesis is that the track is a real pion.

Pionicity $Wobs(K) - Wobs(\pi)$. Comparison between the pion hypothesis and the kaon hypothesis. Positive values for this variable means that the track is more likely to be a pion rather than a kaon.

Kaonicity $Wobs(\pi) - Wobs(K)$. This is the opposite to pionicity.Positive values for this variable means that the track is more likely to be a kaon rather than a pion.

4.2 Data Selection

4.2.1 Skim Three

The first step for any analysis in this experiment is to select the data sub-sample that contains the events to be studied. In our case, we selected the semimuonic (FSAA) sub-sample that came out from Skim Two since it contains events with at least one muon and a meson in the final state. This semimuonic sub-sample was then passed through yet another selection stage, Skim Three. The cuts applied during this skim were very soft cuts in order to prevent the massive loss of good events in this early selection stage.

Skim Three was designed to select events which had a muon plus two opposite charge mesons in the secondary vertex. The mesons could be either two pions (ρ^0), two kaons (ϕ) or a pion and a kaon ($\overline{K^{*0}}$). Muons that were detected in the Inner Muon System with momentum greater than 10 GeV were selected, while for the Outer Muon System the minimum momentum was 4 GeV. The muon CL for the track had to be greater than 0.5%.

The meson identification was done using the information from the Čerenkov through the CITADL algorithm. The pion or pions in the events were required to have $\pi_{\rm con} > -7$. Tracks with kaonicity > -1 were identified as kaons. Once the two mesons and the muon were identified, the secondary vertex was formed. The minimum CL and L/σ separation for a secondary vertex was 1% and 5 respectively. The highest multiplicity primary vertex was selected after the tracks assigned to the secondary vertex were excluded from the search. If more than one vertex had the same multiplicity, then the vertex most upstream of the detector was selected.

Events that passed all the above cuts were then divided into three different samples according to their meson combinations and stored in magnetic tapes for later analysis. After the process was finished, we had three $\overline{K^{*0}}$ tapes, two ρ^0 tapes and one ϕ tape. Each of

these sub-samples was much easier to work with than the whole set of 26 tapes from the FSAA sub-sample.

4.2.2 Skim Four

The last step before the final event selection was called Skim Four. During this skim, each sub-sample from Skim Three was analyzed independently. Basically, all major cuts from Skim Three remained untouched, but at this stage we calculate the invariant mass for each decay mode and imposed some constrain on those masses.

The output of these analyses were stored in Ntuples which are $N_{events} \times N_{variables}$ arrays where N_{events} is the number of events that passed all skim cuts and $N_{variables}$ is the number of variables stored per event. Each Ntuple was then processed using PAW++, a software developed at CERN for data analysis and presentation. The biggest advantage of using PAW is that the analysis can be done interactively allowing the change of different parameters without the need of compiling and running a Fortran program each time a change is made.

Figure 4.1 shows the mass distributions for all events that passed skim4. It should be note that, while for $\overline{K^{*0}}$ there is a clear signal, the ρ^0 signal is buried beneath heavy background. This is easy to understand since there are a lot of resonances with two-pion final-states and two-pions plus neutral particles final-states that contribute to $D^+ \rightarrow \rho^0\mu^+\nu$ background. This makes the $D^+ \rightarrow \rho^0\mu^+\nu$ analysis more complicated than $D^+ \rightarrow \overline{K^{*0}}\mu^+\nu$ analysis.

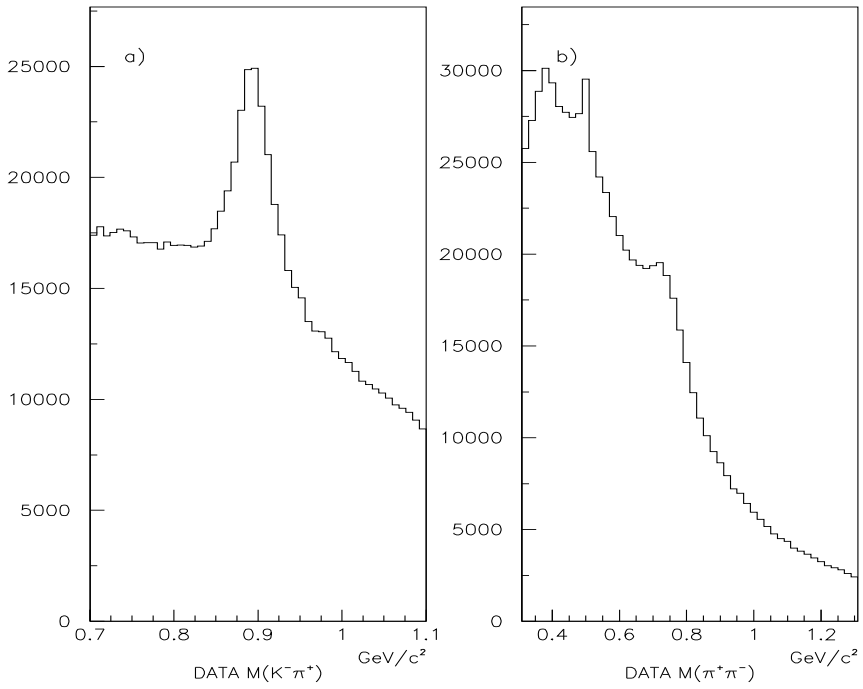

Figure 4.1: Invariant mass distributions for all events that passed Skim Four. a) $D^+ \to \overline{K^{*0}}\mu^+\nu$ candidates, b) $D^+ \to \rho^0\mu^+\nu$ candidates.

4.3 Analysis

4.3.1 $D^+ \to \overline{K^{*0}}\mu^+\nu$

$D^+ \to \overline{K^{*0}}\mu^+\nu$ events were reconstructed after requiring a secondary vertex with a $K^-\pi^+\mu^+$ track combination [1] with a confidence level (CLS) greater than 10% and $Iso2 < 1.0\%$. In order to get a cleaner charm signal, the secondary vertex was constrained to be outside the target material by 1σ and to have L/$\sigma > 20$.

The primary vertex was reconstructed after eliminating the tracks already assigned to the secondary vertex from the search. The primary with the highest multiplicity was

[1] Throughout this thesis, charge conjugation is implicitly assumed.

chosen. If two primry vertices have the same multiplicity, the vertex most upstream of the spectrometer was chosen. The minimum confidence level for this vertex (CLP) was 1% and $Iso1 < 1\%$.

The muon candidate was required to have $CL_{imu} > 1\%$ with momentum greater than 10 GeV. We used only inner muons in this analysis. Kaon candidates with kaonicity greater than 2 and pions with $\pi_{\rm con}$ greater than -7 were accepted.

Events with $K^-\pi^+\mu^+$ charge combination were called Right Sign (RS), while events with $K^+\pi^-\mu^+$ charge combination were called Wrong Sign (WS). WS events were used to model combinatoric background. This combinatoric background arises when a kaon track and a pion track that do not form a real vertex are mistakenly assigned to the secondary vertex. Before performing the fit, we subtracted WS events from RS events because in that way we eliminate combinatoric background that by chance happen to have the correct charge combination.

Another source of background are events with the following decay chain: $D^{*+} \rightarrow D^0\pi^+, D^0 \rightarrow K^-\mu^+\nu$, where the pion from the primary vertex is erroneously assign to the secondary vertex. This kind of background can be suppressed with a cut on the invariant mass difference $M(K^-\pi^+\mu^+) - M(K^-\mu^+) > 0.20 GeV/c^2$. Contamination from other semileptonic D^+ and D_s decays were reduced when we selected events with a cut on the visible invariant mass $M(K^-\pi^+\mu^+)$. The cut used was $1.0 < M(K^-\pi^+\mu^+) < 1.8$.

After all the above cuts were applied and background subtraction was performed, we saw no evidence for residual contamination from other resonances in the $D^+ \rightarrow \overline{K^{*0}}\mu^+\nu$ signal (Figure 4.3).

The $D^+ \rightarrow K^-\pi^+\pi^+$ signal was used as the normalization mode. This mode was selected because its topology is very similar to that of the $D^+ \rightarrow \overline{K^{*0}}\mu^+\nu$. In order to

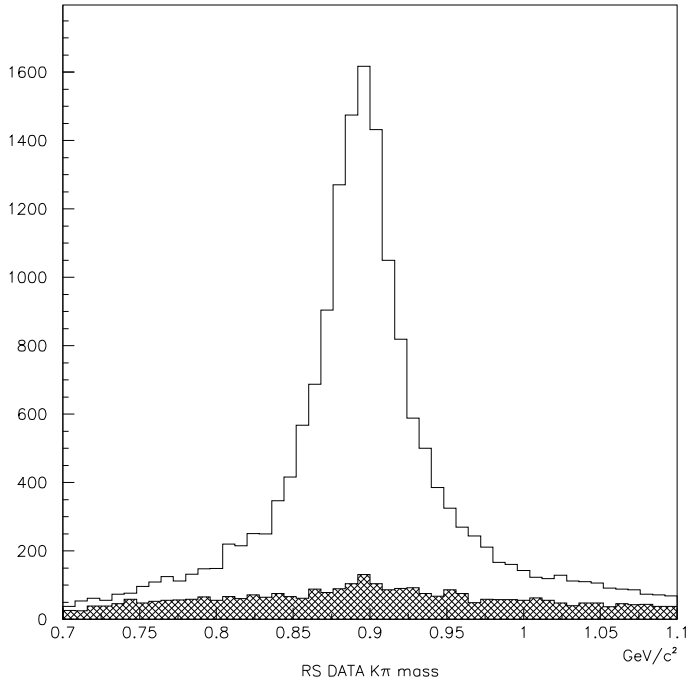

Figure 4.2: Right Sign (solid histogram) and Wrong Sign events (hatched histogram) for events that passed all analysis cuts. The Wrong Sign events are subtracted from Right Sign events.

reduce common systematic errors, the cuts used for $D^+ \to K^-\pi^+\pi^+$ were equal to those of $D^+ \to \overline{K^{*0}}\mu^+\nu$ whenever possible.

The $D^+ \to \overline{K^{*0}}\mu^+\nu$ branching ratio relative to $D^+ \to K^-\pi^+\pi^+$ was calculated using the following:

$$\frac{BR(D^+ \to \overline{K^{*0}}\mu^+\nu)}{BR(D^+ \to K^-\pi^+\pi^+)} = \frac{Y_{D^+\to\overline{K^{*0}}\mu^+\nu}/\epsilon_{D^+\to\overline{K^{*0}}\mu^+\nu}}{Y_{D^+\to K^-\pi^+\pi^+}/\epsilon_{D^+\to K^-\pi^+\pi^+}} \times \frac{1}{BR(\overline{K^{*0}} \to K^-\pi^+)} \qquad (4.1)$$

where Y corresponds to Yield and the ϵ represent efficiencies. The efficiencies were calculated using events generated with FOCUS Monte Carlo simulation (MCFOCUS).

$$\epsilon = \frac{N_{obs}}{N_{gen}} \tag{4.2}$$

where N_{obs} is the number of events that passed all the analysis cuts and N_{gen} is the number of events generated in the simulation. All Monte Carlo events were subjected to exactly the same selection criteria as the real data.

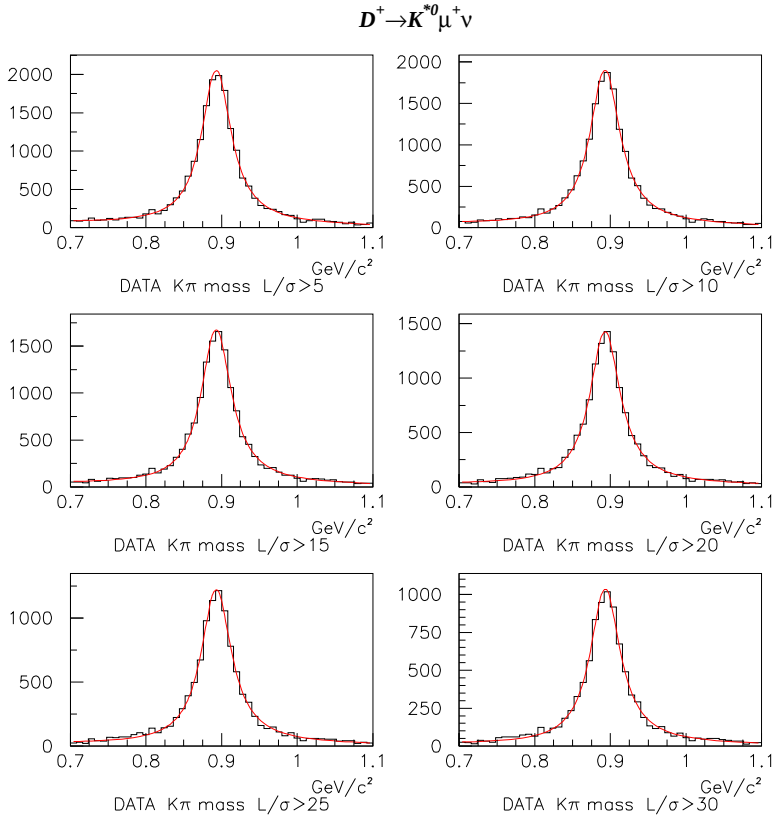

Figure 4.3: M($K^-\pi^+$) plots for events that passed all analysis cuts. The L/σ value was varied from 5 to 30. The fit was done with a Breit Wigner line shape

4.3.2 $D^+ \to \rho^0 \mu^+ \nu$

As in the case for $D^+ \to \overline{K^{*0}}\mu^+\nu$, we started the $D^+ \to \rho^0\mu^+\nu$ analysis looking for a secondary vertex with two opposite charge pions and a muon outside the target material. This vertex was required to have CLS $> 5\%$ and Iso2 $< 1\%$. The minimum L/σ used was 20. The primary vertex was found in the usual way, excluding the secondary tracks from the search and looking for the vertex with the highest multiplicity. The requirements for this vertex were: CLP $> 1\%$ and Iso1 $< 1\%$.

In order to get a cleaner signal, only muons from the Inner Muon System were used in our analysis. The muon candidate was required to have a momentum greater than 10 and $CL_{imu} > 1\%$. Pion identification was done different for each pion in the vertex depending on the sign of the pion with respect to that of the muon. The pion with the same charge as the muon was required to have pionicity > 0, while the pion with opposite charge as the muon was required pionicity > 5. This was done to reduce the background comming from $D^+ \to \overline{K^{*0}}\mu^+\nu$, $\overline{K^{*0}} \to K^-\pi^+$, where the kaon is misidentified as a pion. as mentioned before, the charge of this kaon is always opposite to the charge of the muon. Monte Carlo studies have shown, that this cut can keep the "efficiency" for $\overline{K^{*0}}$ events in our signal area well below 0.01%, while keeping the ρ^0 efficiency high. Figure 4.4 show the efficiency as a function of the pion identification cut.

Backgrounds from $D^{*0} \to D^0\pi^+, D^0 \to \pi^-\mu^+\nu$, were suppressed requiring a minimal invariant mass difference $M(\pi^+\pi^-\mu^+) - M(\pi^-\mu^+) > 0.20$ (as in $D^+ \to \overline{K^{*0}}\mu^+\nu$), while other semileptonic decays that will be discuss later, were reduced with a cut in the invariant mass of the three charge tracks, $1.2 < M(\pi^+\pi^-\mu^+) < 1.8$. These semileptonic decays, along with their efficiencies for these mass cuts, are shown in Table 4.1. The usefulness of the $M(\pi^+\pi^-\mu^+) - M(\pi^-\mu^+)$ cut is demonstrated in Figure 4.7. Events where one of the pion comes from the primary, but it is erroneously assigned to the secondary, can effectively eliminated with the use of this cut.

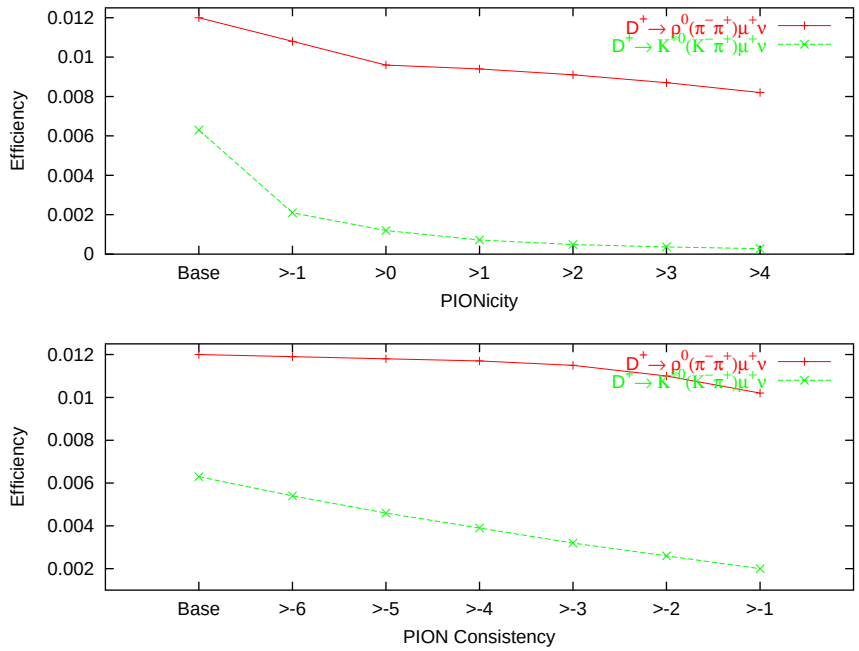

Figure 4.4: Efficiency for $D^+ \to \rho^0\mu^+\nu$ compared to $D^+ \to \overline{K^{*0}}\mu^+\nu$ after applying different pion identification cuts for the pion with charge opposite to the charge of the muon. All other cuts used in the analysis have been applied.

Decay Mode	Mass Difference	Three-body	Both Cuts
$D^+ \to \rho^0\mu^+\nu$	96%	76%	73%
$D^+ \to \overline{K^{*0}}\mu^+\nu, K/\pi Mis-id$	85%	57%	43%
$D^+ \to \eta\mu\nu, \eta \to \pi\pi\pi^0$	71%	29%	25%
$D^+ \to \eta\mu\nu, \eta \to \pi\pi\gamma$	75%	40%	33%
$D_s^+ \to \eta'\mu\nu, \eta' \to \rho^0\gamma$	96%	67%	65%
$D_s^+ \to \eta'\mu\nu, \eta' \to \eta\pi\pi$	67%	5%	5%
$D_s^+ \to \eta\mu\nu, \eta \to \pi\pi\pi^0$	73%	39%	34%
$D_s^+ \to \eta\mu\nu, \eta \to \pi\pi\gamma$	78%	49%	42%

Table 4.1: Efficiencies for some semimuonic decays after mass cuts were applied. Mass Difference refers to $M(\pi^+\pi^-\mu^+) - M(\pi^-\mu^+) > 0.20$, while Threebody refers to $1.2 < M(\pi^+\pi^-\mu^+) < 1.8$. When neither mass cut is applied, the efficiency is 100%.

In contrast to the $D^+ \to \overline{K^{*0}}\mu^+\nu$ case, the WS events that modeled our combinatoric background were defined as the events where the two pions have the same sign. In this case,

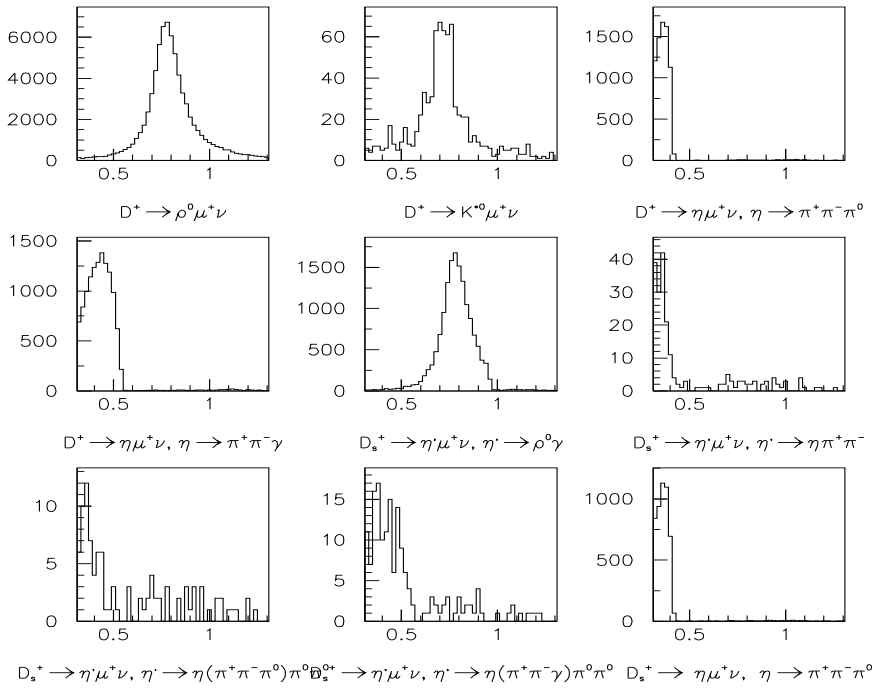

Figure 4.5: Some semileptonic contributions to $D^+ \to \rho^0 \mu^+ \nu$. These semileptonic decays were chosen because all of them have at least two pions in the final state.

we did not subtract them from the RS events; instead, we use the shape of this background in our fit which I'll discuss in the next section.

The last source of background comes from muon misidentification. This kind of contamination comes most of the time from pions that decay to muons. To assess the amount of muon misidentification, we took a sub-sample of approximately 10 % of the FOCUS data and performed the same analysis but with opposite muon requirements (e.g.,. $CL_{imu} < 1\%$) and plot $M(\pi^+\pi^-)$. Then, we weighted this histogram with a momentum dependent misidentification probability function and boosted it by the ratio of the amount of charm decays in the full sample to the amount of charm decays in our sub-sample [2].

[2]For a complete discussion on Muon Mis-Id and how it is calculated, see [22]

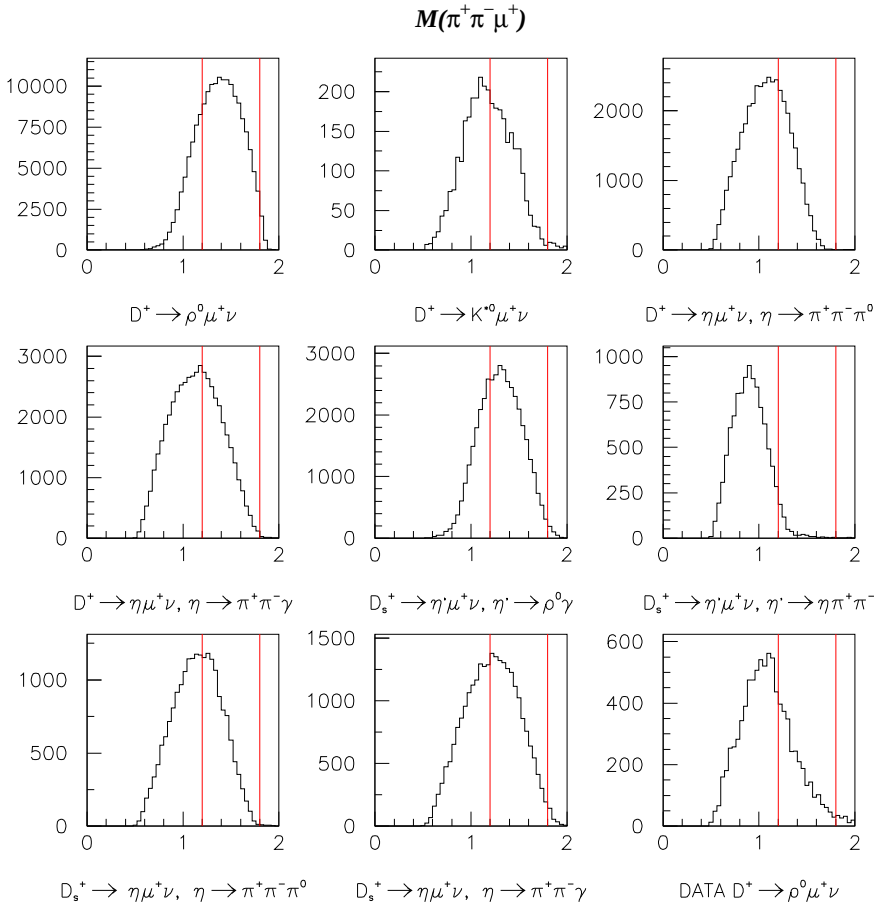

Figure 4.6: Plots for the variable $M(\pi^+\pi^-\mu^+)$ for the semileptonic contributions. The vertical lines represent the final cut applied. All other cuts have been applied.

The normalization mode used was $D^+ \rightarrow \overline{K^{*0}}\mu^+\nu$. This choice is due to the similarities that both decay modes have. Except for the identification cuts, all other cuts applied to the $D^+ \rightarrow \rho^0\mu^+\nu$ sample were applied to the normalization sample. This will reduce common systematic uncertainties.

The $D^+ \rightarrow \rho^0\mu^+\nu$ branching ratio relative to $D^+ \rightarrow \overline{K^{*0}}\mu^+\nu$ was calculated using :

$$\frac{BR(D^+ \rightarrow \rho^0\mu^+\nu)}{BR(D^+ \rightarrow \overline{K^{*0}}\mu^+\nu)} = \frac{Y_{D^+\rightarrow\rho^0\mu^+\nu}/\epsilon_{D^+\rightarrow\rho^0\mu^+\nu}}{Y_{D^+\rightarrow\overline{K^{*0}}\mu^+\nu}/\epsilon_{D^+\rightarrow\overline{K^{*0}}\mu^+\nu}} \times BR(\overline{K^{*0}} \rightarrow K^-\pi^+) \qquad (4.3)$$

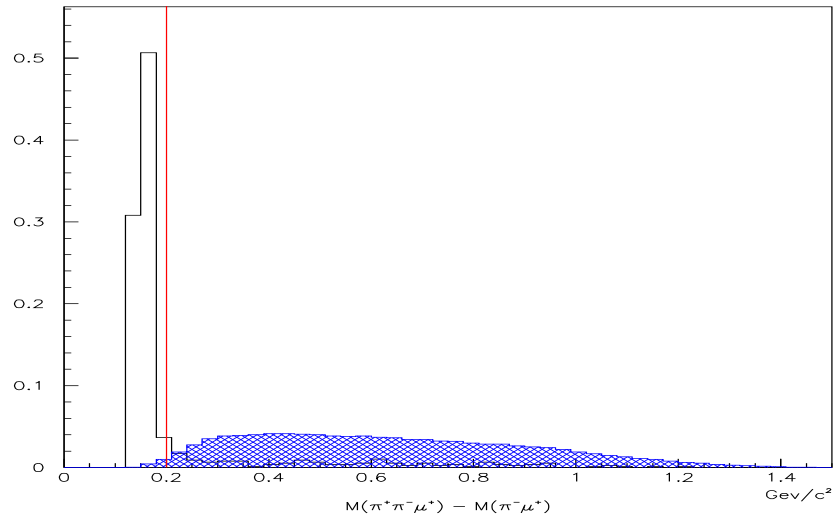

Figure 4.7: $M(\pi^+\pi^-\mu^+) - M(\pi^-\mu^+)$ for $D^{*0} \to D^0\pi^+, D^0 \to \pi^-\mu^+\nu$ events (solid histogram) compared to $D^+ \to \rho^0\mu^+\nu$ events (hatched histogram). Both distribution are normalize to unity. The vertical line represents the cut we are applying to our data.

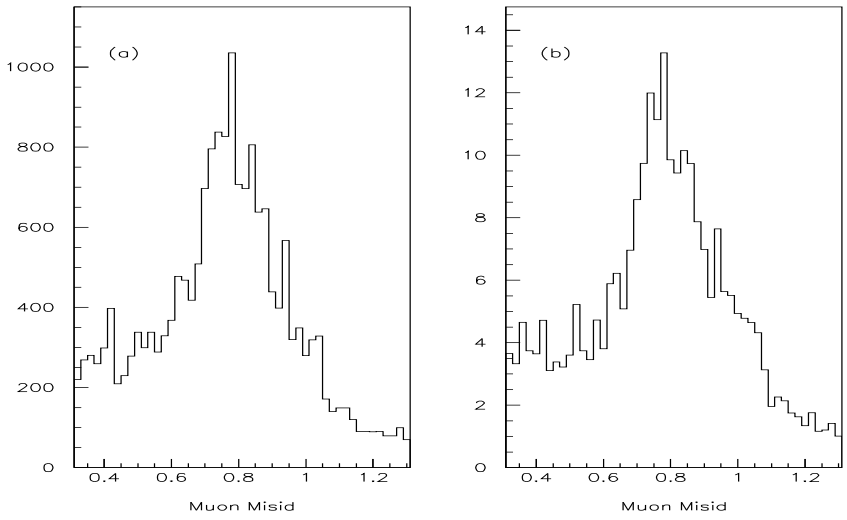

Figure 4.8: Backgroung from Muon Mis-Id. Effects of momentum dependent weighting function ((a) before weight, (b) after weight) in the muon mis-id background distribution. This weighted distribution (b) was used in our fit.

The $D^+ \rightarrow \rho^0\mu^+\nu$ yield for the branching ratio was calculated using a *binned maximum log likelihood* technique discussed in the next section, while the $D^+ \rightarrow \overline{K^{*0}}\mu^+\nu$ yield was estimated fitting with a Breit Wigner line shape. The efficiencies were calculated from Monte Carlo samples using equation (4.2).

4.4 Fitting Technique

$D^+ \rightarrow \rho^0\mu^+\nu$ signal is not an easy signal to deal with. The difficulties in extracting the yield arises because there are many different sources of background, each of which peaks just below the ρ^0 peak. This makes it very difficult to estimate the background present with the use of sidebands. To solve this problem, instead of trying to know the function that describes the signal and the background, we try to estimate the number of events that enter our data histogram from all the sources that can contribute to it. For this, we need to know which are the possible backgrounds that in principle can contaminate our data.

Our $D^+ \rightarrow \rho^0\mu^+\nu$ yield was estimated using a binned maximum likelihood technique, where we are trying to predict the number of events from each source that are present in each bin. The semimuonic background sources in Table 4.1 either have two pions in the final state, or two pions plus a neutral particle in the final state.

The likelihood was constructed as:

$$\mathcal{L} = \prod_{i=1}^{\#bins} \frac{n_i^{s_i} e^{-n_i}}{s_i!} \tag{4.4}$$

where:

s_i =number of events in bin i of data histogram;

n_i =number of events in bin i of fit histogram.

The fit histogram was composed of the following:

1. $D^+ \to \rho^0\mu^+\nu$ signal, whose shape was given by the Monte Carlo and the yield was a fit parameter.

2. Feed-through from $D^+ \to \overline{K^{*0}}\mu^+\nu$, $(K/\pi Mis - id)$ with shape given by Monte Carlo and the yield depended on the value calculated in $D^+ \to \overline{K^{*0}}\mu^+\nu$ analysis using a Breit Wigner line shape.

3. $D^+ \to \eta\mu\nu, \eta \to \pi\pi\pi^0$, with shape given by Monte Carlo and the yield was a parameter of the fit.

4. $D^+ \to \overline{K^0}\mu^+\nu$, with shape given by Monte Carlo and yield determined as a fit parameter.

5. $D^+ \to \eta\mu\nu, \eta \to \pi\pi\gamma$, with shape given by Monte Carlo and the yield depended on $Y_{D^+\to\eta\mu\nu,\eta\to\pi\pi\pi^0}$ through $\frac{BR(\eta\to\pi\pi\gamma)}{BR(\eta\to\pi\pi\pi^0)}$.

6. Various backgrounds from $D_s^+ \to \eta'\mu\nu$ and $D_s^+ \to \eta\mu\nu$, whose yields depended on $D_s^+ \to \phi\mu^+\nu$ efficiency corrected yield and on the PDG [23] values for $\frac{BR(D_s^+\to\eta'\mu\nu)}{BR(D_s^+\to\phi\mu\nu)}$ and $\frac{BR(D_s^+\to\eta\mu\nu)}{BR(D_s^+\to\phi\mu\nu)}$ respectively.

7. $D_s^+ \to \phi\mu^+\nu$, $\phi \to \rho^0\pi^0$, with shape determined by Monte Carlo and yield depend on $D_s^+ \to \phi\mu^+\nu$ efficiency corrected yield and on the PDG value for BR($\phi \to \rho^0\pi^0$).

8. Combinatoric background, with shape given by same sign pions from the data.

9. Muon Mis-Id, with shape given by data and yield was fixed in the fit.

The number of entries in bin *i* of the fit histogram was defined as:

$$
\begin{aligned}
n_i =& Y_{\rho\mu\nu} S_{1i} + \frac{Y_{\overline{K^{*0}}\mu^+\nu}}{\epsilon(\overline{K^{*0}}\mu^+\nu)} \epsilon(\overline{K^{*0}}\mu^+\nu \to \rho\mu\nu) S_{2i} + \\
& Y_{D^+\to\eta\mu\nu,\eta\to\pi\pi\pi^0} \left[S^a_{3i} + \frac{BR(\eta\to\pi\pi\gamma)}{BR(\eta\to\pi\pi\pi^0)} \frac{\epsilon(\eta\to\pi\pi\gamma)}{\epsilon(\eta\to\pi\pi\pi^0)} S^b_{3i} \right] + \\
& Y_{D^+\to\overline{K^0}\mu\nu} S_{4i} + \frac{Y_{D_s^+\to\phi\mu^+\nu}}{\epsilon(D_s^+\to\phi\mu^+\nu) BR(\phi\to KK)} BR(\phi\to\rho^0\pi^0) S_{5i} \\
& \frac{Y_{D_s^+\to\phi\mu^+\nu}}{\epsilon(D_s^+\to\phi\mu^+\nu) BR(\phi\to KK)} \Big\{ BR_{\eta'} \cdot \Big[BR(\eta'\to\rho\gamma)\epsilon(\eta'\to\rho\gamma) S_{6i} + \\
& BR(\eta'\to\eta\pi\pi)\epsilon(\eta'\to\eta\pi\pi) S_{7i} \Big] + BR_\eta \cdot \big(BR(\eta\to\pi\pi\pi^0)\epsilon(\eta\to\pi\pi\pi^0) S_{8i} + \\
& BR(\eta\to\pi\pi\gamma)\epsilon(\eta\to\pi\pi\gamma) S_{9i} \big) \Big\} + \mathcal{C} S_{10i} + \mathcal{M} S_{11i}
\end{aligned}
\tag{4.5}
$$

where:

$Y_{\rho\mu\nu}$ is the fitted yield for $D^+ \to \rho^0\mu^+\nu$; $\frac{Y_{\overline{K^{*0}}\mu^+\nu}}{\epsilon(\overline{K^{*0}}\mu^+\nu)}$ is the efficiency corrected yield for $D^+ \to \overline{K^{*0}}\mu^+\nu$; $Y_{D^+\to\eta\mu\nu,\eta\to\pi\pi\pi^0}$ is the fitted yield for $D^+ \to \eta\mu\nu$; $BR_{\eta'} = \frac{BR(D_s^+\to\eta'\nu)}{BR(D_s^+\to\phi e\nu)}$; $BR_\eta = \frac{BR(D_s^+\to\eta e\nu)}{BR(D_s^+\to\phi e\nu)}$; $Y_{D^+\to\overline{K^0}\mu\nu}$ is the fitted yield for $D^+ \to \overline{K^0}\mu\nu$; $\mathcal{C}$ is the fitted Combinatoric Background; $\mathcal{M}$ is the fixed Muon Mis-Id; S_i are normalized Monte Carlo shapes and BR are Branching Ratios from PDG. The signal was fitted using the range from 0.31MeV/c^2 to 1.31MeV/c^2.

Chapter 5

Results

In this chapter we will present the results for the semileptonic branching ratios $\frac{\Gamma(D^+\to\overline{K^{*0}}\mu^+\nu)}{\Gamma(D^+\to K^-\pi^+\pi^+)}$ and $\frac{\Gamma(D^+\to\rho^0\mu^+\nu)}{\Gamma(D^+\to\overline{K^{*0}}\mu^+\nu)}$.

5.1 $D^+ \to \overline{K^{*0}}\mu^+\nu$

5.1.1 Fit Results

The yield for $D^+ \to \overline{K^{*0}}\mu^+\nu$ was calculated after we fitted the M(Kπ) histogram using a Breit Wigner line shape. In general the line shape of a resonance with total angular momentum j can be written as:

$$f(M) = \frac{\Gamma}{(2\pi)(M-m_0)^2 + (\Gamma/2)^2}; \Gamma = \Gamma_0 \left(\frac{p^*}{p_0^*}\right)^{2j+1}$$

where Γ is the width of the resonance, p^* is the momentum of the K in the Kπ rest frame and the 0 subscript refers to the the value when M(Kπ)=M(K^*).

For the purpose of our fit, we used a constant width Breit Wigner line shape, i.e.

$\Gamma = \Gamma_0$ plus a polynomial function that describes our residual background. The parameters of our fitting function were the yield, the mass and the width of the $K\pi$ system. We also fitted the signal using both S-wave Breit Wigner ($2j+1=1$) and P-wave Breit Wigner ($2j+1=3$) and saw that our result did not suffer any significant change. This was later used to determine any bias coming from our fitting technique. After the fit, we found a total of 15265 ± 124 $D^+ \to \overline{K^{*0}}\mu^+\nu$ candidates, where the error quoted is the error returned by MINUIT, our minimization software.

The $D^+ \to K^-\pi^+\pi^+$ normalization mode was fitted with the use of a Gaussian line shape plus a polynomial function describing the background remaining after all the analysis cuts. As in the $D^+ \to \overline{K^{*0}}\mu^+\nu$ case, the number of $D^+ \to K^-\pi^+\pi^+$ candidates was calculated integrating the signal area. We found a total of 72426 ± 264 candidates.

Using the above results, along with the efficiencies for both decay modes, we calculated:

$$\frac{\Gamma(D^+ \to \overline{K^{*0}}\mu^+\nu)}{\Gamma(D^+ \to K^-\pi^+\pi^+)} = 0.595 \pm 0.008$$

where the uncertainty quoted at this stage is only statistical. This result includes a correction factor of 0.945 due to the s-wave interference term reported by FOCUS [24] in the $D^+ \to K^-\pi^+\mu^+\nu$ system.

5.1.2 Systematic Errors

We used several analysis techniques to assess systematic biases in our measurement. Because the normalizing modes in the branching ratios have nearly the same topology as the decays studied, most of the systematic uncertainties should cancel when the ratio is taken. Our analysis concludes that after the ratio is taken, the only systematic sources left are due to the fitting technique and the final cut selection.

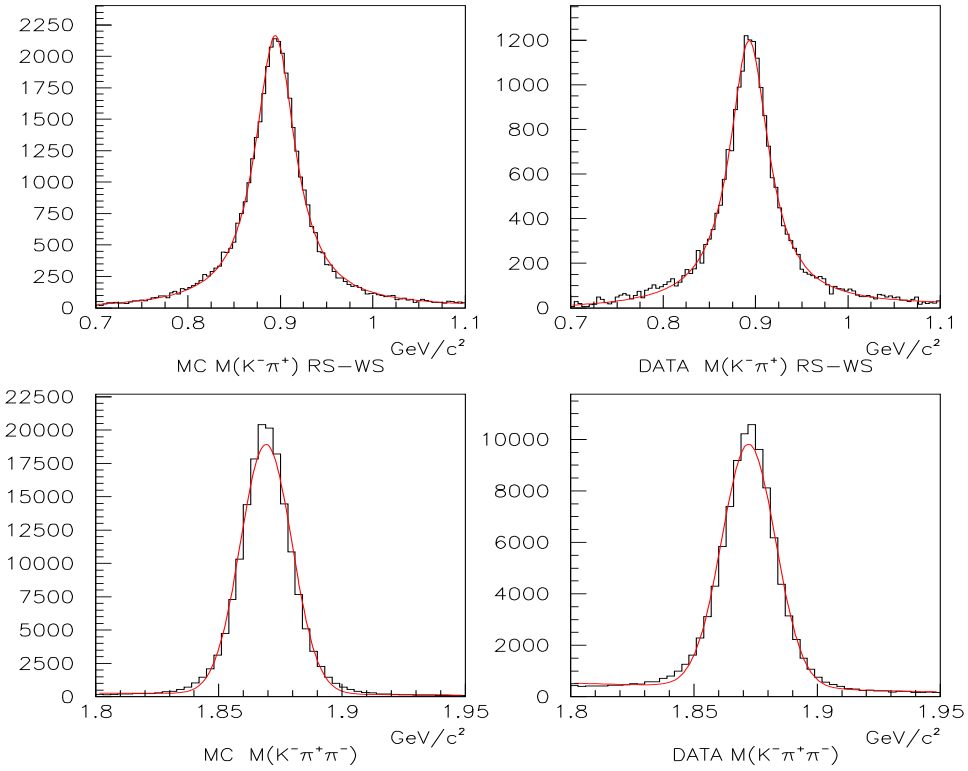

Figure 5.1: $D^+ \to \overline{K^{*0}}\mu^+\nu$ and $D^+ \to K^-\pi^+\pi^+$ mass plots. In all plots, the fit result is superimposed on the histograms.

Uncertainties due to our fitting technique can be studied performing N reasonable changes to the fit and recalculating the branching ratio for each change. The systematic uncertainty associated with these variations is just the variance of the measurements [25]:

$$\sigma_{syst} = \sqrt{\frac{\sum_{i=1}^{N} x_i^2 - N < x >^2}{N-1}} \tag{5.1}$$

where $< x >$ is the average branching ratio.

Table 5.3 summarizes the different studies made to calculate systematic errors. For these studies, we change both the bin size in the histogram as well as the mass range used for our fit. As mentioned before, we also studied the effect of the selected line shape used

in our fit. We recalculate the branching ratio using a S-Wave Breit Wigner and a P-Wave Breit Wigner. It is important to note that although we did not find any significant difference in the branching ratio with the use of different Breit Wigner parameterizations, studies of the exact $D^+ \to \overline{K^{*0}}\mu^+\nu$ line-shape are currently underway by the Brazil Group within the FOCUS collaboration and a paper addressing this matter is expected soon. The calculated variance for these fit variations was 0.009

Systematic uncertainty due to the final cut selection was studied recalculating the branching ratio for different cuts. For this purpose we change the values for the secondary vertex CL, secondary isolation, kaonicity and out of target cuts. We then calculate the variance for all these cuts (72 cut combinations) and use this value as the error due to the cut selection. We found this variance to be 0.008. Table 5.1 and Table 5.2 summarize the changes made to calculate the systematic uncertainties.

Adding these sources of systematic uncertainties in quadrature we state a final result of:

$$\frac{\Gamma(D^+ \to \overline{K^{*0}}\mu^+\nu)}{\Gamma(D^+ \to K^-\pi^+\pi^+)} = 0.595 \pm 0.008(stat) \pm 0.014(syst)$$

Cut	Cut Variation
CL_{sec}	$> 0.1, 0.15, 0.20$
Iso2	$< 0.01, 0.005, 0.001$
Out of Target	$> 0, 1, 2, 3$
Kaonicity	$> 2, 5$

Table 5.1: $D^+ \to \overline{K^{*0}}\mu^+\nu$ Cut Variations

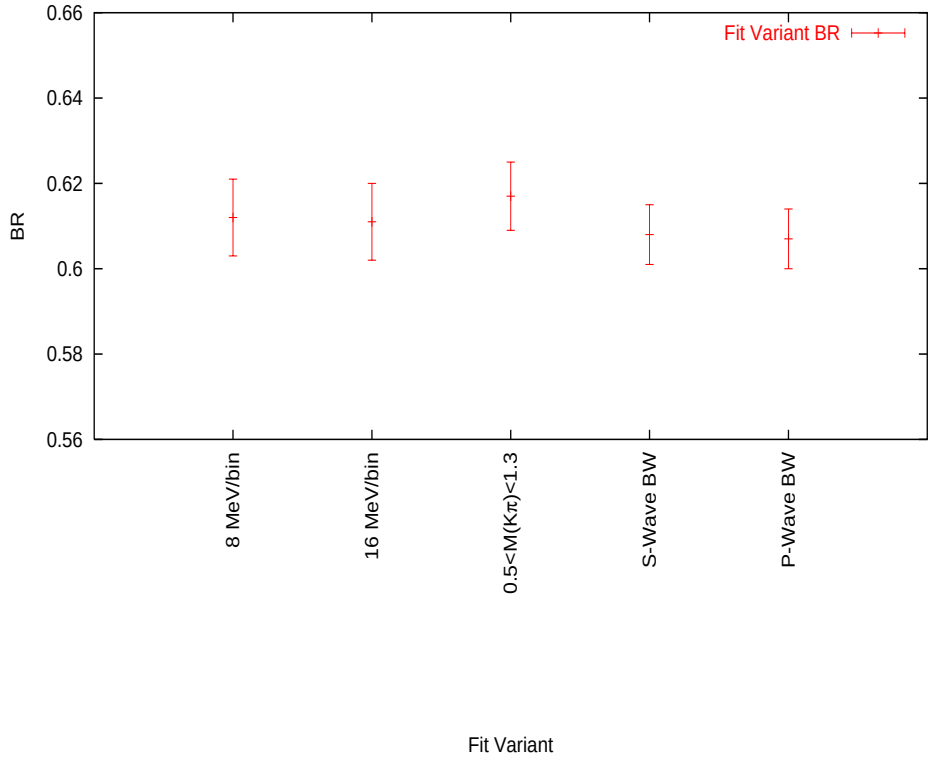

Figure 5.2: $\frac{\Gamma(D^+ \to \overline{K^{*0}} \mu^+ \nu)}{\Gamma(D^+ \to K^- \pi^+ \pi^+)}$ Fit Variants. Branching ratio for various fit variations.

Fit Variation	$\frac{\Gamma(D^+ \to \overline{K^{*0}} \mu^+ \nu)}{\Gamma(D^+ \to K^- \pi^+ \pi^+)}$
8MeV/bin ($0.7 \leq M(K\pi) \leq 1.1$)	0.612 ± 0.009
16MeV/bin ($0.7 \leq M(K\pi) \leq 1.1$)	0.611 ± 0.009
($0.5 \leq M(K\pi) \leq 1.3$)	0.617 ± 0.008
S-wave Breit Wigner line shape	0.607 ± 0.007
P-wave Breit Wigner line shape	0.608 ± 0.007

Table 5.2: $D^+ \to \overline{K^{*0}} \mu^+ \nu$ Fit Variants. Variations in the fit for systematic uncertainty determination.

5.2 $D^+ \to \rho^0 \mu^+ \nu$

5.2.1 Fit Results

The yield for $D^+ \to \rho^0 \mu^+ \nu$ was extracted using the technique described in Section 4.4. From equation (4.5), it can seen that in order to estimate the amount of

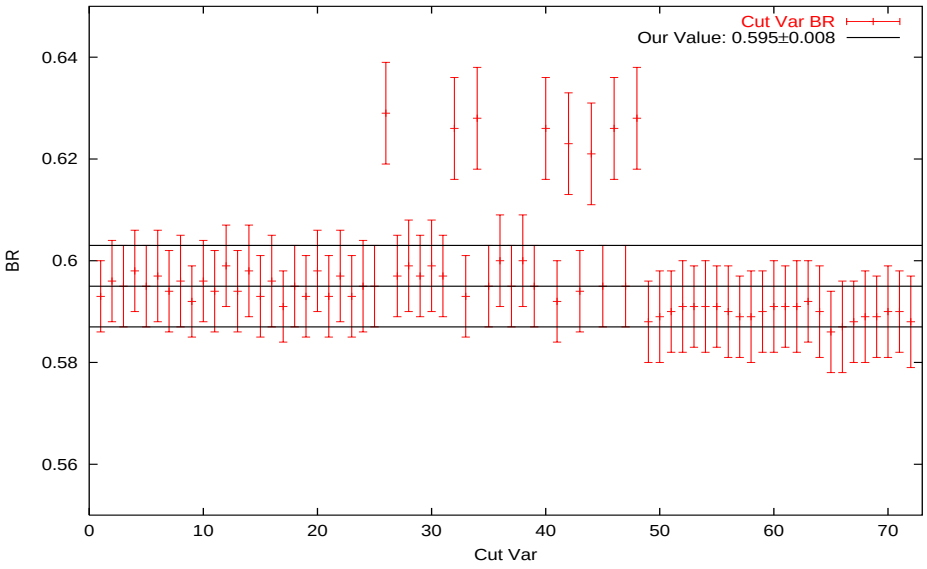

Figure 5.3: $\frac{\Gamma(D^+ \to \overline{K^{*0}}\mu^+\nu)}{\Gamma(D^+ \to K^-\pi^+\pi^+)}$ Cut variations. Branching ratio for 72 cut combinations. The horizontal lines represent the branching ratio value and 1σ for standard set of cuts.

Syst. Source	σ_{syst}
line shape	0.007
fit variants	0.009
cut variations	0.008
Total Syst	0.014

Table 5.3: $D^+ \to \overline{K^{*0}}\mu^+\nu$ Systematic Sources

background from decays such as $D_s^+ \to \eta'\mu\nu$ and $D_s^+ \to \eta\mu\nu$, we need to know the number of $D_s^+ \to \phi\mu^+\nu$ that were produced in FOCUS. $D_s^+ \to \phi\mu^+\nu$ candidates, where the ϕ decays into two kaons, were reconstructed using the cuts in Table 5.4.

Vertex	Particle ID	Mass
$L/\sigma > 5$	$Wobs(\pi) - Wobs(K^+) > 2$	$0.985 \leq M_\phi \leq 1.085$
$CLS > 1\%$, $Iso2$ <%	$Wobs(\pi) - Wobs(K^-) > 2$	
$CLP > 1\%$, $Iso1$ <%	$CL_\mu > 1\%$	

Table 5.4: Cuts applied to $D_s^+ \to \phi\mu^+\nu$ candidates

The $D_s^+ \to \phi\mu^+\nu$ yield was calculated after the mass histogram was fitted using a

Breit Wigner line-shape plus a polynomial function. The total of $D_s^+ \to \phi\mu^+\nu$ candidates reconstructed was 1316 ± 47. The mass histograms are shown in Figure 5.4.

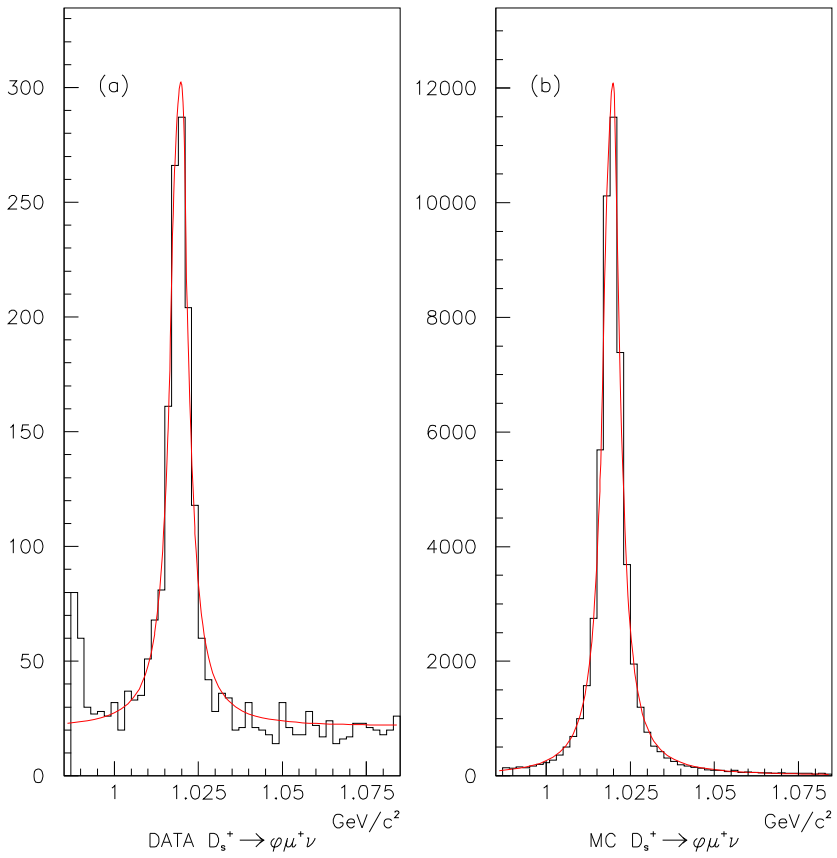

Figure 5.4: $D_s^+ \to \phi\mu^+\nu$ mass plots. Figure (a) shows the data histogram, while figure (b) shows our MC simulation. The fitting function is superimposed on both histograms.

Using the result from $Y_{D_s^+ \to \phi\mu^+\nu}$, we performed the Binned Maximum Log Likelihood fit. We found a total of 189 ± 28 $D^+ \to \rho^0\mu^+\nu$ candidates. The results of the fit are presented in Table 5.5 along with the contributions from the semileptonic decays with two pions in the final state and non-charm background. Figure 5.5 shows the fitted histograms.

Decay Mode	Yield
$D^+ \to \rho^0\mu^+\nu$	189
$D^+ \to \overline{K^{*0}}\mu^+\nu, K/\pi Mis-id$	50
$D^+ \to \eta\mu\nu, \eta \to \pi\pi\pi^0$	< 1
$D^+ \to \eta\mu\nu, \eta \to \pi\pi\gamma$	< 1
$D^+ \to \overline{K^0}\mu\nu$	13
$D_s^+ \to \eta'\mu\nu, \eta' \to \rho^0\gamma$	71
$D_s^+ \to \eta'\mu\nu, \eta' \to \eta\pi\pi$	2
$D_s^+ \to \eta\mu\nu, \eta \to \pi\pi\pi^0$	53
$D_s^+ \to \eta\mu\nu, \eta \to \pi\pi\gamma$	17
$D_s^+ \to \phi\mu^+\nu, \phi \to \rho\pi$	22
Muon Mis-Id	255
Combinatoric	234

Table 5.5: Semileptonic Contributions to $D^+ \to \rho^0\mu^+\nu$ signal

We used the fitted yield along with the MC efficiencies to calculate $\frac{\Gamma(D^+\to\rho^0\mu^+\nu)}{\Gamma(D^+\to\overline{K^{*0}}\mu^+\nu)}$. We found:

$$\frac{\Gamma(D^+ \to \rho^0\mu^+\nu)}{\Gamma(D^+ \to \overline{K^{*0}}\mu^+\nu)} = 0.034 \pm 0.005$$

Looking at the fitted histogram in Figure 5.5(a), it is clear that we can fit fairly well all the mass range except for the peak around $0.9 \leq M_{\pi\pi} \leq 1.0$. This background, which is not accounted for, is most probably a real two-pion decay. Preliminary studies showed that these events are long lived and have high muon confidence level. This indicated to us that these events are most likely coming from a D^+ candidate. The only known particle with a two-pion final state around that mass range is the $f_0(980)$, but the process $D^+ \to f_0\mu^+\nu$ has never been observed. Although this decay process seems to be the best candidate, a very detailed analysis has to be done before any claim can be made. It is important to note that even though we have not included this decay in our fit, we do not expect the branching ratio to change significantly if this source is added since the excess of events in this region is $\sim 1\%$ of all the events.

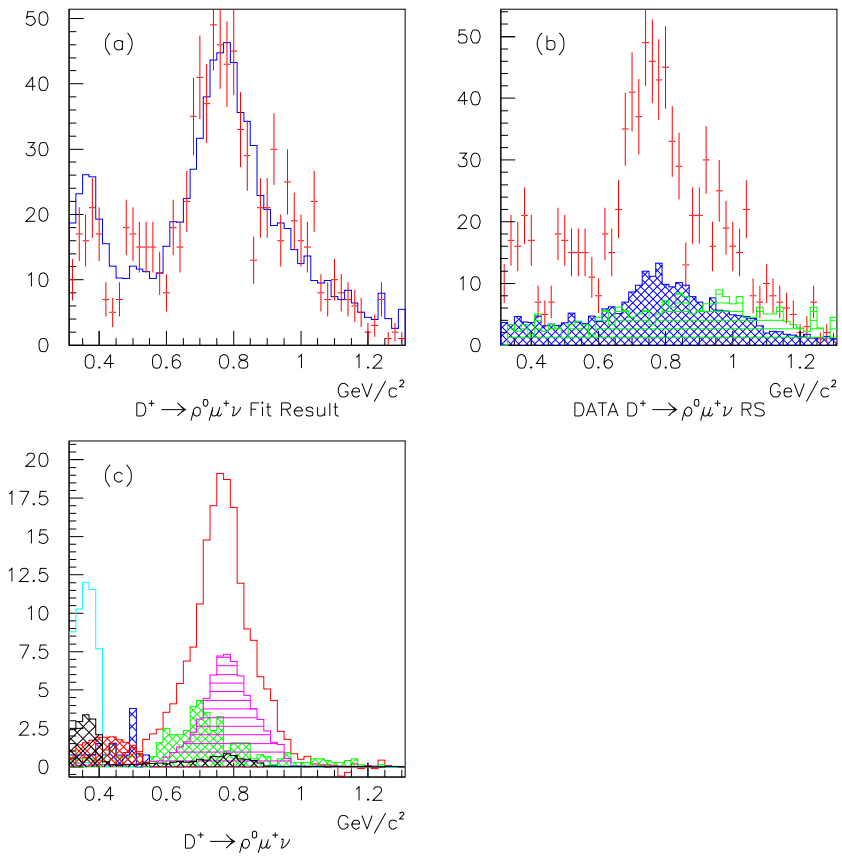

Figure 5.5: Binned maximum log likelihood fit results. Figure (a) shows the fit result (solid histogram) over the data histogram (with error bars). Figure (b) shows the contributions from WS (horizontal bars) and Muon-Misid (hatched) events. Semileptonic contributions listed in Table 4.1 are shown in figure (c).

5.2.2 Systematic Errors

To calculate the systematic uncertainties in our branching ratio measurement, we used the same technique employed in our previous analysis. We looked at systematic errors due to both fitting technique and cut selection.

The uncertainty due to the fitting technique was calculated with the use of different

studies. One study looked at the effect of the bin size and mass range used in the fit. To study the effect due to the branching ratios used in equation (4.5), we varied the value of each branching ratio over $\pm 1\sigma$. Another fit variation was the use of a Breit Wigner fitting function to extract the yield, instead of our preferred method using a binned maximum log likelihood. Table 5.7 and Figure 5.6 summarizes all the tests made. Using equation (5.1) we quote a systematic uncertainty due to our fitting technique of: $\sigma_{syst} = 0.004$.

As we did for the $D^+ \to \overline{K^{*0}}\mu^+\nu$ case, the systematic uncertainty due to the cut selection was studied recalculating the branching ratio for different cut combinations. In these studies, we change the value for the secondary vertex CL, secondary isolation, out of material cut and the pionicity of the pion with opposite charge to that of the muon. In total, we studied 108 cut combinations (Figure 5.7). The systematic uncertainty associated with these cut variations is, as the case for the fit variants, the variance of measured branching ratios. We quote a systematic uncertainty due to the cut selection of: $\sigma_{syst} = 0.003$. Combining these two systematic uncertainties in quadrature we have:

$$\frac{\Gamma(D^+ \to \rho^0 \mu^+ \nu)}{\Gamma(D^+ \to \overline{K^{*0}}\mu^+\nu)} = 0.034 \pm 0.005(stat) \pm 0.005(syst)$$

This new measurement represents a big improvement in the branching ratio determination. The amount of statistics (~ 5 times more than E687) give us the most precise result for this decay mode.

It is important to note that the above result does not include the correction factor due to the s-wave interference in the $D^+ \to K^-\pi^+\mu^+\nu$ system. The inclusion of such term implies a shift of $+0.4\sigma$ in all our results. In the remainder of the discussion, we will quote the result without this correction factor.

Cut	Cut Variation
CL_{sec}	$> 0.05, 0.10, 0.15$
Iso2	$< 0.01, 0.005, 0.001$
Out of Target	$> 0, 1, 2, 3$
Pionicity	$> 3, 5, 8$

Table 5.6: $D^+ \to \rho^0 \mu^+ \nu$ Cut Variations. The pionicity cut is applied only to the pion with charge opposite to the muon.

Fit Variation	$\frac{\Gamma(D^+ \to \rho^0 \mu^+ \nu)}{\Gamma(D^+ \to \overline{K^{*0}} \mu^+ \nu)}$
10 MeV/bin ($0.31 \leq M(\pi\pi) \leq 1.31$)	0.034 ± 0.007
40 MeV/bin ($0.31 \leq M(\pi\pi) \leq 1.31$)	0.033 ± 0.007
($0.50 \leq M(\pi\pi) \leq 1.10$)	0.027 ± 0.009
Fitted Muon Mis-Id	0.035 ± 0.007
$BR's + 1\sigma$	0.028 ± 0.007
$BR's - 1\sigma$	0.038 ± 0.007
BW Fit	0.035 ± 0.003

Table 5.7: $D^+ \to \rho^0 \mu^+ \nu$ Fit Variants. Variations in the fit for systematic uncertainty determination.

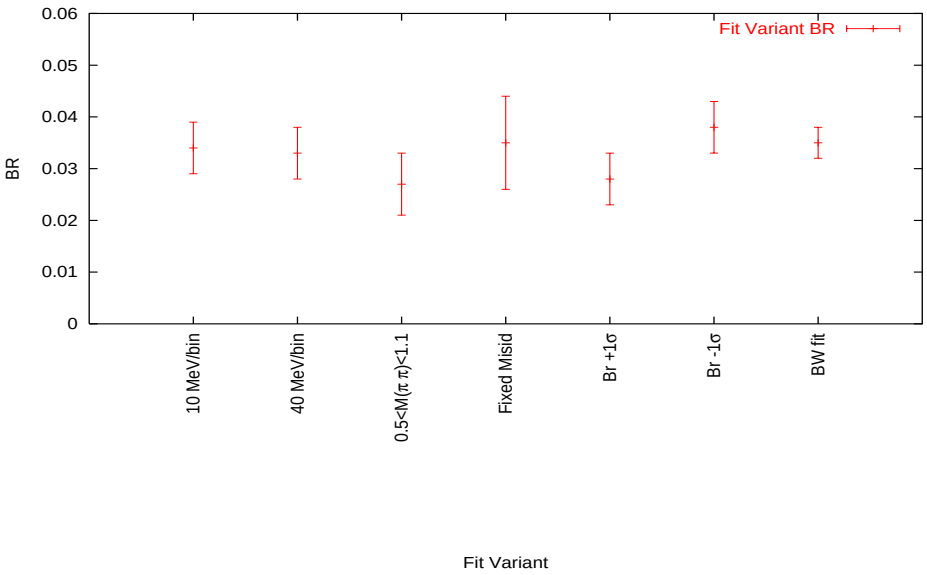

Figure 5.6: $\frac{\Gamma(D^+ \to \rho^0 \mu^+ \nu)}{\Gamma(D^+ \to \overline{K^{*0}} \mu^+ \nu)}$ Fit Variants. Branching ratio for various fit variations.

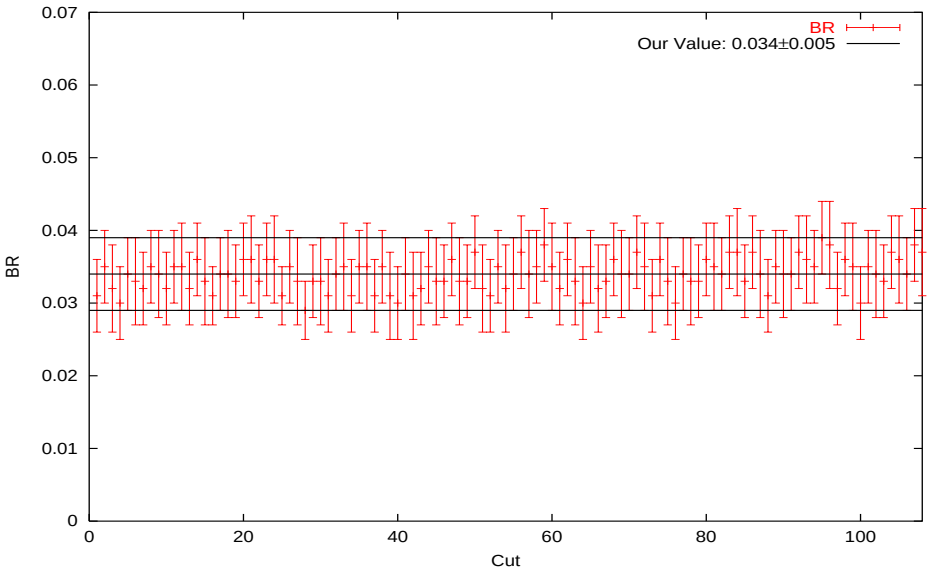

Figure 5.7: $\frac{\Gamma(D^+\to\rho^0\mu^+\nu)}{\Gamma(D^+\to\overline{K^{*0}}\mu^+\nu)}$ Cut variations. Branching ratio for 108 cut combinations. The horizontal lines represent the branching ratio value and 1σ for our standard set of cuts.

Syst. Source	σ_{syst}
fit variants	0.003
cut variations	0.004
Total Syst	0.005

Table 5.8: $D^+ \to \rho^0\mu^+\nu$ Systematic Sources

5.3 Decay Rates

Using the measured branching ratios, we can calculate the decay rates for both semileptonic processes. The first step to get the decay rate is to calculate the rate of the semileptonic process with respect to all D's. Then, using the D^+ lifetime, the total decay rate can be calculated.

$$\frac{\Gamma(D^+ \to Vl^+\nu)}{\Gamma_{total}} = \frac{\Gamma(D^+ \to Vl^+\nu)}{\Gamma(NormalizingMode)} \times \frac{\Gamma(NormalizingMode)}{\Gamma_{total}} \tag{5.2}$$

$$\Gamma(D^+ \to Vl^+\nu) = \frac{\Gamma(D^+ \to Vl^+\nu)}{\Gamma_{total}} \times \frac{1}{\tau_{D^+}} \tag{5.3}$$

Using $\frac{\Gamma(D^+ \to K^-\pi^+\pi^+)}{\Gamma_{total}} = 0.091 \pm 0.006$ from PDG2002 and the new FOCUS result for the D^+ lifetime [26]: $\tau_{D^+} = (1039.4 \pm 4.3) \times 10^{-15}$ sec, we calculated:

$$\frac{\Gamma(D^+ \to \overline{K^{*0}}\mu^+\nu)}{\Gamma_{total}} = 0.054 \pm 0.004$$

$$\Gamma(D^+ \to \overline{K^{*0}}\mu^+\nu) = (5.19 \pm 0.38) \times 10^{10} sec^{-1}$$

where we have added in quadrature the statistical and systematic uncertainty of the $\frac{\Gamma(D^+ \to \overline{K^{*0}}\mu^+\nu)}{\Gamma(D^+ \to K^-\pi^+\pi^+)}$ to calculate the uncertainty in our calculation. Furthermore, if we multiply our measured branching ratio by a phase space factor of 1.05 [23], we can calculate $\Gamma(D^+ \to \overline{K^{*0}}l^+\nu)$:

$$\frac{\Gamma(D \to \overline{K^{*0}}l^+\nu)}{\Gamma_{total}} = 0.057 \pm 0.004$$

$$\Gamma(D \to \overline{K^{*0}}l^+\nu) = (5.48 \pm 0.39) \times 10^{10} sec^{-1}$$

Using the above results, we quote:

$$\frac{\Gamma(D^+ \to \rho^0\mu^+\nu)}{\Gamma_{total}} = 0.0018 \pm 0.0004$$

$$\Gamma(D^+ \to \rho^0\mu^+\nu) = (0.17 \pm 0.03) \times 10^{10} sec^{-1}$$

In the next Chapter, these results will be compared to previous experiments and theoretical predictions. Also, the implications of these results on the world average will be discussed.

Chapter 6

Conclusions

6.1 Comparison with Previous Experiments

Since the decay process $D^+ \rightarrow \overline{K^{*0}}\mu^+\nu$, has been studied thoroughly, we can compare our results with previous experiments. ALL these experiments have already been discussed in Chapter Two. Table 6.1 summarizes the previous results.

Experiment	$\frac{\Gamma(D^+\rightarrow\overline{K^{*0}}\mu^+\nu)}{\Gamma(D^+\rightarrow K^-\pi^+\pi^+)}$	$\Gamma(D^+ \rightarrow \overline{K^{*0}}\mu^+\nu)(10^{10}sec^{-1})$
E653 (1992)	$0.46 \pm 0.07 \pm 0.08$	
E687 (1993)	$0.56 \pm 0.04 \pm 0.06$	
PDG (2000)	0.53 ± 0.06	4.53 ± 0.38
CLEO (2002)	$0.72 \pm 0.10 \pm 0.06$	6.31 ± 0.71
E831 (2002)	$0.602 \pm 0.010 \pm 0.021$	
This Result (2003)	$0.595 \pm 0.008 \pm 0.014$	5.19 ± 0.38

Table 6.1: $\frac{\Gamma(D^+\rightarrow\overline{K^{*0}}\mu^+\nu)}{\Gamma(D^+\rightarrow K^-\pi^+\pi^+)}$ Experimental Results

Our $\frac{\Gamma(D^+\rightarrow\overline{K^{*0}}\mu^+\nu)}{\Gamma(D^+\rightarrow K^-\pi^+\pi^+)}$ measurement is consistent with all previous experimental results. Furthermore, this measurement is an independent confirmation of the result published by FOCUS last year [27].

The decay process $D^+ \to \rho^0 \mu^+ \nu$ is a different case than that of $D^+ \to \overline{K^{*0}} \mu^+ \nu$ since only two experiments have been able to observe it. Due to the small statistics available in those experiments, the uncertainties in the measurement are big. Our measured $\frac{\Gamma(D^+ \to \rho^0 \mu^+ \nu)}{\Gamma(D^+ \to \overline{K^{*0}} \mu^+ \nu)}$ is smaller than the present world average by about 2σ, but as I will discuss in the next section, it is consistent with the theoretical predictions for this mode. Including our result, the new world average will be $\frac{\Gamma(D^+ \to \rho^0 \mu^+ \nu)}{\Gamma(D^+ \to \overline{K^{*0}} \mu^+ \nu)} = 0.040 \pm 0.008$. This represents a significant improvement in the branching ratio determination.

Experiment	$\frac{\Gamma(D^+ \to \rho^0 \mu^+ \nu)}{\Gamma(D^+ \to \overline{K^{*0}} \mu^+ \nu)}$	$\Gamma(D^+ \to \rho^0 \mu^+ \nu)(10^{10} sec^{-1})$
E791 (1997)	$0.051 \pm 0.015 \pm 0.009$	0.22 ± 0.09
E687 (1997)	$0.079 \pm 0.019 \pm 0.013$	
PDG (2000)	0.061 ± 0.014	
This Result (2003)	$0.034 \pm 0.005 \pm 0.005$	0.17 ± 0.03

Table 6.2: $\frac{\Gamma(D^+ \to \rho^0 \mu^+ \nu)}{\Gamma(D^+ \to \overline{K^{*0}} \mu^+ \nu)}$ Experimental Results

6.2 Comparison with Theoretical Models

There are various theoretical models that can predict both branching ratios and decay rates for different semileptonic processes. In this section, I will compare the results obtained in this work with the predicted values made by some of these models.

The first model to which our results are compared is the ISGW2 [28] model. ISGW2 is an update of the ISGW quark model for semileptonic meson decays. It incorporate *heavy quark symmetry*. Among the many important features of this model it should be mention that it include the heavy quark symmetry constraints on the relations between the form factors away from zero recoil ($q^2 = q^2_{max}$) and on the slope of the form factors near zero recoil.

In their publication, the authors calculated the partial decay rates for most of the

semileptonic modes decaying from D and B mesons including $D^+ \to \overline{K^{*0}}\mu^+\nu$ and $D^+ \to \rho^0\mu^+\nu$. They predicted the $D^+ \to \rho^0\mu^+\nu$ to $D^+ \to \overline{K^{*0}}\mu^+\nu$ branching ratio to be 0.023.

A *relativistic constituent quark* model proposed by Wolfgang Jaus [29] also predicted the rates for semileptonic decays of D and B mesons. The model make use of *vector meson dominance* to calculate the q^2 dependence of the form factors. The author predicted the $D \to K^* l\nu$ rate to be $5.5 \times 10^{10} sec^-1$ and the $D^+ \to \rho^0\mu^+\nu$ to $D^+ \to \overline{K^{*0}}\mu^+\nu$ branching ratio to be 0.030.

The last model to which our results will be compared is a model by O'Donnell and Turan [6]. They used the *light-front* quark model to determined the ratio of form factors $\frac{|A_0^{D\to\rho}|}{|A_0^{D\to K^*}|}$ at the kinematic point where $q^2 = 0$. This ratio is often taken to be unity by SU(3)-flavor symmetry. The authors calculated this ratio to be 0.88. Using this value, they predicted the branching ratio of $D^+ \to \rho^0\mu^+\nu$ to $D^+ \to \overline{K^{*0}}\mu^+\nu$ to be 0.025.

Table 6.3 and Table 6.4 summarize the predictions by these theoretical models and compare them to our results. It is clear that the predictions of these models are in fairly good agreement with our measured branching ratios and decay rates.

Model	$\Gamma(D^+ \to \overline{K^{*0}} l\nu)(10^{10} sec^{-1})$
ISGW2	5.4
Jaus	5.5
This Thesis (2003)	5.48 ± 0.39

Table 6.3: $\frac{\Gamma(D^+\to\overline{K^{*0}}\mu^+\nu)}{\Gamma(D^+\to K^-\pi^+\pi^+)}$ Theoretical Predictions

Model	$\frac{\Gamma(D^+\to\rho^0\mu^+\nu)}{\Gamma(D^+\to\overline{K^{*0}}\mu^+\nu)}$	$\Gamma(D^+ \to \rho^0\mu^+\nu)(10^{10} sec^{-1})$
ISGW2	0.023	0.12
Jaus	0.030	
O'Donnell & Turan	0.025	
This Thesis (2003)	$0.034 \pm 0.005 \pm 0.005$	0.17 ± 0.03

Table 6.4: $\frac{\Gamma(D^+\to\rho^0\mu^+\nu)}{\Gamma(D^+\to\overline{K^{*0}}\mu^+\nu)}$ Theoretical predictions

6.3 Possible Extensions of this Work

There are several studies and measurements possible using data from FOCUS that can be performed in the near future. The first and most important is the determination of the Form Factors associated for the decay process $D^+ \to \rho^0 \mu^+ \nu$. There is a special interest from the scientific community for this result since this measurement has never been made before and will probe the underlying hadronic structure of the decay. For this to be done, we will need to have a very clean signal in order to avoid contamination in the kinematic variables due to backgrounds.

Another important study remaining is the identification of the background in the mass range $0.9 \leq M_{\pi\pi} \leq 1.0$. This background, which may hint at a new decay process, has to be studied and fully understood so we can have a better understanding of the $M_{\pi\pi}$ line shape.

References

[1] A. Bandyopadhayay et al., "Impact of the first SNO results on Neutrino Mass and Mixing," *Phys. Lett. B*, vol. 519, p. 83, 2001.

[2] Donald H. Perkins, *Introduction to High Energy Physics*. Cambridge University Press, 4th ed., 2000.

[3] M. Kobayashi and T. Maskawa, "CP Violation in the Renormalizable Theory of Weak Interaction," *Prog. Theor. Phys.*, vol. 49, p. 652, 1973.

[4] F. J. Gilman and R. L. Singleton, "Analysis of Semileptonic Decays of Mesons Containing Heavy Quarks," *Phys. Rev. D*, vol. 41, p. 140, 1990.

[5] J. D. Richman and P. R. Burchart, "Leptonic And Semileptonic Decays of Charm and Bottom Hadrons," *Rev. Mod. Phys.*, vol. 67, p. 893, 1995.

[6] P. J. O'Donnell and G. Turan, "Charm and Bottom Semileptonic Decays," *Phys. Rev. D*, vol. 56, p. 295, 1997.

[7] P. L. Frabetti et al., "Description and Performance of the Fermilab E687 Spectrometer," *Nucl. Instrum. Methods A*, vol. 320, p. 519, 1992.

[8] P. L. Frabetti et al., "Analysis Of The Decay Mode $D^+ \to \overline{K^{*0}}\mu^+\nu$," *Phys. Lett. B*, vol. 307, p. 262, 1993.

[9] P. L. Frabetti et al., "Observsation of the Vector Meson Cabbibo Suppressed Decay $D^+ \to \rho^0 \mu^+ \nu$," *Phys. Lett. B*, vol. 391, p. 235, 1997.

[10] J. C. Anjos et al., "Measurement of the Form Factors in the decay $D^+ \to \overline{K^{*0}} e^+ \nu$," *Phys. Rev. Lett.*, vol. 65, p. 2360, 1990.

[11] K. Kodama et al., "Measurement of the Form Factor ratios in the decay $D^+ \to \overline{K^{*0}} \mu^+ \nu$," *Phys. Lett. B*, vol. 274, p. 246, 1992.

[12] K. Kodama et al., "Measurement of the Branching Ratio for $D^+ \to \overline{K^{*0}} \mu^+ \nu$," *Phys. Lett. B*, vol. 286, p. 187, 1992.

[13] E. M. Aitala et al., "Measurement of the Form Factor Ratio for $D^+ \to \overline{K^{*0}} l^+ \nu_l$," *Phys. Lett. B*, vol. 440, p. 435, 1998.

[14] E. M. Aitala et al., "Measurement of the Branching Ratio $\frac{D^+ \to \rho^0 l^+ \nu_l}{D^+ \to \overline{K^{*0}} l^+ \nu_l}$," *Phys. Lett. B*, vol. 397, p. 325, 1997.

[15] CLEO Collaboration, "Measurement of the $D^+ \to \overline{K^{*0}} l \nu$ Branching Fraction," *Phys. Rev. Lett.*, vol. 89, p. 222001, 2002.

[16] John Cumalat, "Choice of Target Material," E831 Internal Memo, unpublished.

[17] J. M. Link et al., "The Target Silicon Detector for the FOCUS Spectrometer," *hep-ex/0204023*, 2002.

[18] Richard Fernow, *Introduction to Experimental Particle Physics*. Cambridge University Press, 1986.

[19] J. M. Link et al., "Čerenkov Identification in FOCUS," *Nucl. Instrum. Methods A*, vol. 484, p. 270, 2002.

[20] J. D. Jackson, *Classical Electrodynamics*. John Wiley & Sons, 2nd ed., 1975.

[21] R. K. Bock and W. Krischer, *Particle Detector Briefbook*. Springer Verlag, 1999. http://rkb.home.cern.ch/rkb/titleD.html.

[22] Hugo Hernandez, "A Search for the Rare Decay $D^0 \rightarrow \mu^+\mu^-$," Master's thesis, University of Puerto Rico, Mayaguez, Puerto Rico, July 2001.

[23] Particle Data Group *The European Physical Journal C*, vol. 15, 2000.

[24] J. M. Link et al., "Evidence for New Interference Phenomena in the Decay $D^+ \rightarrow K^-\pi^+\mu^+\nu$," *Phys. Lett. B*, vol. 535, p. 43, 2002.

[25] R. Gardner, J. E. Wiss, "Estimating Systematics Errors," E831 Internal Memo, unpublished, 1994.

[26] J. M. Link et al., "New Measurement of the D^0 and D^+ lifetimes," *Phys. Lett. B*, vol. 539, p. 192, 2002.

[27] J. M. Link et al., "New Measurement of the $\frac{\Gamma(D^+\rightarrow\overline{K^{*0}}\mu^+\nu)}{\Gamma(D^+\rightarrow K^-\pi^+\pi^+)}$ and $\frac{\Gamma(D_S^+\rightarrow\phi\mu^+\nu)}{\Gamma(D_S^+\rightarrow\phi\pi^+)}$," *Phys. Lett. B*, vol. 541, p. 243, 2002.

[28] N. Igsur and D. Scora, "Semileptonic Meson Decays in the Quark Model: An update," *Phys. Rev. D*, vol. 52, p. 2783, 1995.

[29] W. Jaus, "Semileptonic, Radiative and Pionic decays of B, B* and D, D* Mesons," *Phys. Rev. D*, vol. 53, p. 1349, 1996.